UNIVERSITY OF CALIFORNIA
RIVERSIDE

Optimization of Multi-Functional 1310 nm Spectral-Domain Optical Coherence Tomography (SD-OCT) System and Three-Dimensional Volumetric OCT Image Registration

A Thesis submitted in partial satisfaction
of the requirements for the degree of

Master of Science

in

Bioengineering

by

Junze Liu

March 2018

Thesis Committee:
Dr. B. Hyle Park, Chairperson
Dr. Jin Nam
Dr. William H. Grover

The Thesis of Junze Liu is approved:

_____

_____

_____

Committee Chairperson

University of California, Riverside

ABSTRACT OF THE THESIS

Optimization of Multi-Functional 1310 nm Spectral-Domain Optical Coherence Tomography (SD-OCT) System and Three-Dimensional Volumetric OCT Image Registration

by

Junze Liu

Master of Science, Graduate Program in Bioengineering
University of California, Riverside, March 2018
Dr. B. Hyle Park, Chairperson

Optical coherence tomography (OCT) is a novel and promising imaging technique that has been widely applied in clinical practice and research. Currently advanced spectral-domain OCT is capable for fast generating three dimensional (3D) volumetric image and extracting multi-biological information that has potential uses in disease study. Based on a laboratory-built multi-functional spectral-domain OCT system with center wavelength of 1310 nm, the research goal in this thesis is to solve problems about proper optical characterization method of volumes of *in vivo* biological sample taken at different time points which requires appropriate 3D volume registration and alignment. In this thesis, system optimization is introduced in order to improve OCT signal-to-noise ratio (SNR) and image quality for better image registration performance. Details of a computational-efficient 3D volume alignment based on cross-correlation image registration is discussed. Optical characterization of post-traumatic epilepsy (PTE) is described as an example to

demonstrate the feasibility of the OCT system and to evaluate the image post-processing method in actual neural disease research.

Table of Contents

List of Figures

Chapter 1: Background and theory basis

Section 1.1 Introduction to optical coherence tomography (OCT)

Optical coherence tomography (OCT) is an optical interferometric medical imaging modality that has been widely used in clinical practice and research. Based on low coherence interferometry, OCT can extract information of optical scattering from sub-surface region of tissue and generate depth-resolved tomographic images. [1] OCT uses relatively long wavelength light that allows it to detect light signal reflected from region of depth of 1 ~ 3 mm in scattering medium. The light-based imaging mechanism allows OCT to deliver high resolution cross-sectional images. The axial and lateral spatial resolution of OCT images is on the scale of a few micrometers. Compared to other traditional image techniques such as confocal microscopy, ultrasound imaging and magnetic resonance imaging (MRI), OCT combines high imaging depth and resolution that reveals its potentials in clinical applications.

OCT is able to finish one depth-profile scanning (A-scan) within tens of microseconds. The fast scanning rate significantly reduces the change of sample motion or metabolic activity over time and makes real time three-dimensional (3D) volumetric imaging possible. In addition, OCT minimizes surgical invasion to the sample or subject before and during imaging, and does not require optical, chemical or ionizing radial label in sample preparation. These benefits make OCT an ideal and promise imaging modality in broad and diverse fields including ophthalmology, optometry, cardiology and neuroscience. [2]

OCT is analogous to medical ultrasound imaging. An ultrasound scanner produces ultrasound waves and measures the magnitude and traveling time of echoes returning from tissue sample. Ultrasound images are created by interpreting these echoes to extract depth-resolved information. OCT applies similar pulse-echo imaging principle [1] but uses light as information carrier rather than sound wave. However, it is difficult to measure the traveling time of light signal between its transmitting out and receiving by detector directly, because light travels much faster than sound in media. Therefore, an OCT scanner utilizes low-coherence interferometry (Figure 1.1 (a)) to measure the magnitude and time delay of optical echoes with high sensitivity. Interferometry technique is a classic optical measurement technique that compares two light beams split from one single light source, one light beam backscattered from tissue sample, and the other one reflected from a mirror with known light path length and time delay as reference. This comparison can be performed quantitatively by calculating the correlation or interference between light. The wave interference is strong when the difference between sample light path length and reference path length is less than the coherence length, which is the propagation distance of a coherent light wave maintains a specific degree of coherence. In order to observe the interference only from a short range of path length differences to obtain images with high axial resolution, the coherence length must be shortened. (Figure 1.1 (b)) Since coherence length is inversely proportional to the bandwidth of light spectrum, broad bandwidth (low-coherence) light source is required in OCT. [2], [3] below Once the interference is

measured, the magnitude and time delay of optical echoes can be determined by applying demodulation to the interference signal.

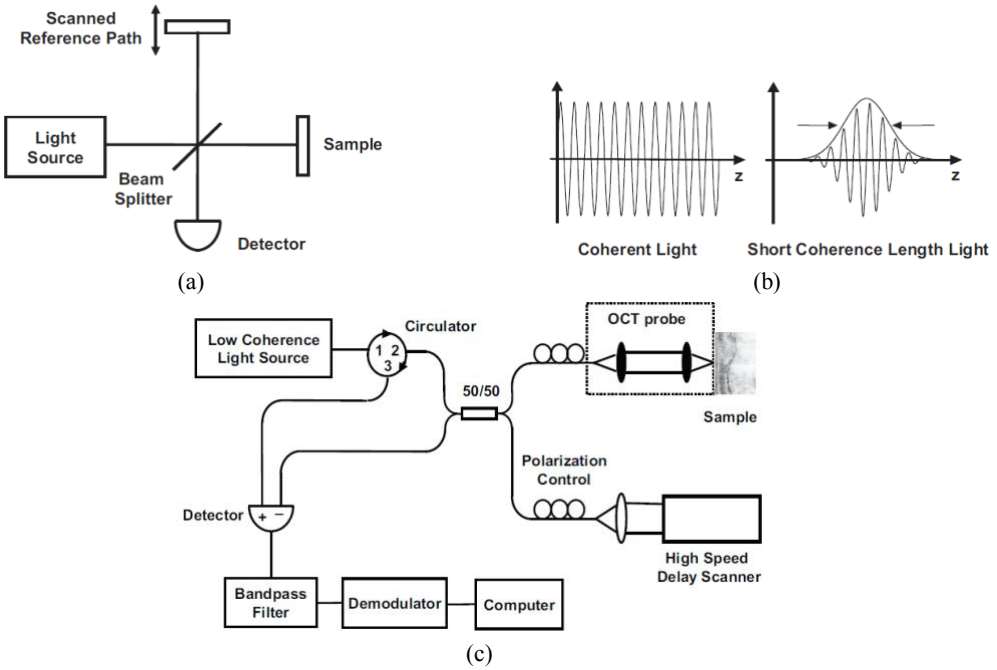

Figure 1.1 Michelson interferometry-based optical coherence tomography. (a) Simplified schematic of low-coherence interferometry with moving reference optical path length. (b) The wave forms of coherent light and short coherence length light. (c) Schematic of early time-domain OCT [2]

Figure 1.1 (c) shows basic working mechanism of a low-coherence interferometry-based time-domain OCT (TD-OCT). Low coherence light is sent out from light source and split into two beams by a beam splitter. The two light beams propagate along two arms, sample arm and reference arm. The sample arm light beam is backscattered from different sub-surface layers of the sample that contains axial information. The reference arm light is reflected by a mirror at the end of a known traveling distance. Both light beams return along the same paths and interfere as they meet. The interference is only observed when the optical path lengths of the sample arm and reference arm are matched in the range

within coherence length because low-coherence light is used. By scanning the reference path over a distance with high speed delay scanner, corresponding depth range of the sample can be imaged. Thus, one depth profile of image can be constructed.

The scanning reference delay arm in conventional TD-OCT produces coherent noise that presents in all wavelengths. OCT imaging speed is then limited by the low signal-to-noise ratio (SNR). This limitation can be overcome by detecting the interference spectrum in Fourier domain. [4] This type of OCT, known as optical frequency domain imaging (OFDI), is equipped with either a spectrometer in the detection arm, or a narrow bandwidth frequency-swept laser light source. The reference arm mirror is fixed in a certain distance and kept stationary. All the echoes of backscattered light are simultaneously measured in the form of spectrum, which eliminates coherent noise. The enhancement in system SNR and sensitivity allows OCT acquiring imaging in a rapid speed.

Section 1.2 Spectral-domain OCT (SD-OCT)

OFDI with a spectrometer is called spectral-domain OCT (SD-OCT). SD-OCT uses similar broad bandwidth low-coherence laser light as its light source, but length of reference arm is stationary and a spectrometer is used in the detection arm (Figure 1.2). When obtaining depth profile, instead of matching the optical path lengths of sample different sub-layers and reference arm by adjusting the position of reference mirror as in TD-OCT, SD-OCT records a Fourier transform of the spectrally-resolved interference fringes, which is the spectrum split by a spectrometer, and reconstructs the depth profile by performing inverse Fourier transform in computer post-processing.

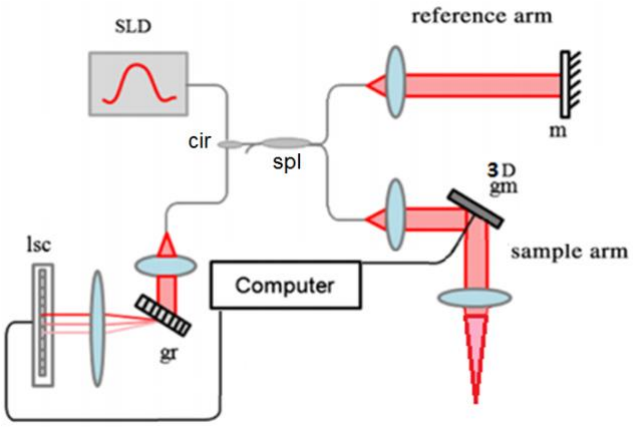

Figure 1.2 Simplified schematic of spectral-domain OCT. A diffraction grating is installed in the detection arm to split light beam into dispersed spectrum and camera converts spectrum signal to electrical current signal for computer processing. SLD: super-luminescent diodes; cir: optical circulator; spl: optical splitter; m: mirror; gm: galvanometer; gr: diffraction grating; lsc: line scanning camera

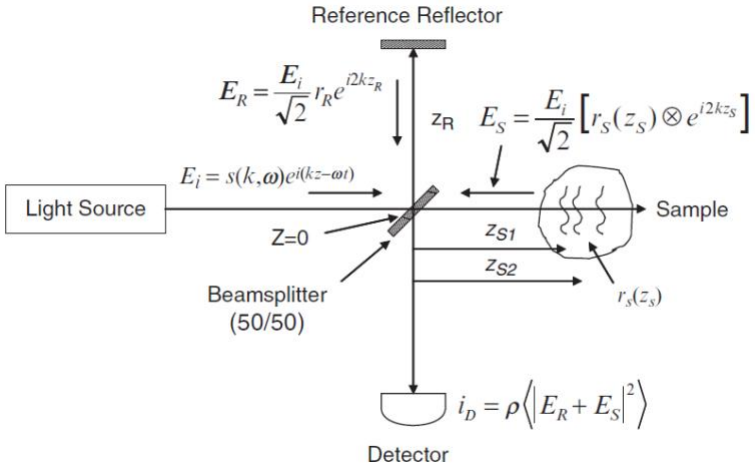

Figure 1.3 Mathematical expression of light power in each part of a Michelson interferometry used in OCT. The "⊗" in sample arm E_s represents convolution operation. [2]

Based on the mathematical description in [2], since the incident light on the Michelson interferometer is considered as polychromatic plane wave, its electric field can be expressed as Eq. 1.1

$$E_i = s(k,\omega)e^{i(kz-\omega t)} \quad \text{Eq. 1.1}$$

where *s(k, ω)* is the electric field magnitude as a function of wavenumber *k* and angular frequency *ω*. Wavenumber *k* is the spatial frequency of a wave defined as $k = 2\pi/\lambda$, where λ is the wavelength. Angular frequency is defined as $\omega = 2\pi v$, where *v* is the frequency of wave. the optical path length along the propagation direction is denoted as *z* while time is denoted as *t*. Assuming the sample is composed of a series of *N* discrete reflectors, the electric fields of returning beams from reference and sample arms are expressed as Eq. 1.2 and Eq. 1.3, respectively

$$E_R = \frac{E_i}{\sqrt{2}} r_R e^{i(2kz_R)} = \frac{s(k,\omega)}{\sqrt{2}} \sqrt{R_R} e^{i(2kz_r-\omega t)} \quad \text{Eq. 1.2}$$

$$E_S = \frac{E_i}{\sqrt{2}} \sum_{n=1}^{N} r_{Sn} e^{i(2kz_{Sn})} = \frac{s(k,\omega)}{\sqrt{2}} \sum_{n=1}^{N} \sqrt{R_{Sn}} e^{i(2kz_{Sn}-\omega t)} \quad \text{Eq. 1.3}$$

where r_R and r_{Sn} are reflectivity of reference arm mirror and the *n*-th ($1 \leq n \leq N$) reflector of sample. The power of each reflector is the magnitude squared of the electric field reflectivity, that is $R_R = |r_R|^2$, and $R_{Sn} = |r_{Sn}|^2$. These two returning fields of optical waves interfere in low coherence interferometer and are received by photocurrent detector. The intensity of photocurrent is proportional to the square of sum of the fields which is given by Eq. 1.4

$$I(k,\omega) = \frac{\rho}{2}(E_R + E_S)^2 \qquad \text{Eq. 1.4}$$

where ρ is the detector sensitivity. Since angular frequency of light wave $\omega = 2\pi\nu$ is significantly greater than the response time of photocurrent detector, the ω term can be reasonably eliminated in the expansion of Eq. 1.4. By using Euler's rule to simplify, the intensity is composed of three main terms as in Eq. 1.5.

$$I(k) = \frac{\rho}{4}\left[S(k)\left(R_R + \sum_{n=1}^{N} R_{Sn}\right)\right] \qquad (1)$$

$$+\frac{\rho}{2}\left[S(k)\sum_{n=1}^{N}\sqrt{R_R R_{Sn}}\cos[2k(z_R - z_{Sn})]\right] \qquad (2)$$

$$+\frac{\rho}{4}\left[S(k)\sum_{n\neq m=1}^{N}\sqrt{R_{Sn}R_{Sm}}\cos[2k(z_{Sn} - z_{Sm})]\right] \qquad (3) \qquad \text{Eq. 1.5}$$

The result of expansion (Eq. 1.5) is composed of three components, "DC terms", "cross-correlation terms", and "auto-correlation terms". DC terms as in Line (1) is the offset to detector current which is independent of pathlength and typically contributes the most to the detector current in SD-OCT system. Cross-correlation terms as in Line (2) is determined by two factors, light source wavenumber *k*, and the optical path length difference between reflectors from sample and reference arm which provides axial position information. Since the mirror in reference arm is stationary, the reflectivity R_R of reference arm can be treated as a constant, and therefore, the cross-correlation is only proportional

to the square root of sample reflectivity of reflector *n* (R_{Sn}) and the cosine of the product of wavenumber and corresponding path length difference. This is the key part in extracting depth information in OCT imaging. Auto-correlation terms in Line (3) is the interference between reflectors in sample. In OCT images, the effect of auto-correlation appears as artifacts which should be minimized by adjusting reference reflectivity R_R in DC and cross-correlation terms so that the auto-correlation effects to the total intensity is relatively small. The sample is usually assumed to be stationary so that the whole auto-correlation can be considered as a constant term (like multiple low-reflectivity "mirrors" stack together). Eq. 1.5 can then be written in a simple form of Eq. 1.6. [2]

$$I(k) = I_r(k) + 2\sqrt{I_r(k)I_s(k)}\sum_{n=1}^{N}\alpha_n \cos(kz_n) + I_s(k) \qquad \text{Eq. 1.6}$$

$I_r(k)$ and $I_S(k)$ are the intensities of reflected light from reference and sample arm, and corresponding to "DC terms" and "auto-correlation terms" in Eq. 1.5, respectively. They are only a function of wavenumber *k* while independent on the axial position z_n. The square root of sample reflectivity at depth z_n is denoted as α_n. The cross-correlation terms are simplified as in the middle term on the right-hand side, which tells the axial depth information.

The optical signal detected by the line scanning camera is the spectrum in Fourier domain. By performing inverse Fourier transform to Eq. 1.6, we can obtain the depth

information of one scanning as different depth positions indicate different light traveling time, and thus, analogous to ultrasound imaging, the traveling time of light signal is feasible to be measured and the "pulse-echo" like imaging principle is implemented. In specific, the following Fourier transform pairs are used to solve the inverse Fourier transform problem.

$$\cos(kz_n) \overset{F}{\leftrightarrow} \frac{1}{2}[\delta(z - z_n) + \delta(z + z_n)]$$

$$1 \overset{F}{\leftrightarrow} \delta(z)$$

Based on the linearity property and convolution theorem of Fourier transform, the inverse Fourier transform can be written as in Eq. 1.7 ~ Eq. 1.9.

$$\mathcal{F}^{-1}[I(k)] = \mathcal{F}^{-1}[I_r(k)] * \left[\delta(z) + \sqrt{\frac{I_s(k)}{I_r(k)}} \sum_{n=1}^{N} \alpha_n[\delta(z - z_n) + \delta(z + z_n)] + O\left(\frac{I_s(k)}{I_r(k)}\right)\right] \quad \text{Eq. 1.7}$$

$$|\mathcal{F}^{-1}[I(k)]|^2 = |\mathcal{F}^{-1}[I_r(k)]|^2 * \left[\delta(z) + \frac{I_s}{I_r} \sum_{n=1}^{N} {\alpha_n}^2[\delta(z - z_n) + \delta(z + z_n)]^2 + +O\left(\frac{{I_s}^2}{{I_r}^2}\right)\right] \quad \text{Eq. 1.8}$$

$$|\mathcal{F}^{-1}[I(k)]|^2 = \Gamma^2(z)$$

$$* \left[\delta(z) + \sum_{n=1}^{N} {\alpha_n}^2 \delta(z - z_n) + \sum_{n=1}^{N} {\alpha_n}^2 \delta(z + z_n) + O\left(\frac{{I_s}^2}{{I_r}^2}\right) \right] \qquad \text{Eq. 1.9}$$

$\Gamma(z)$ is the envelope of the coherence function. This equation presents the axial depth information is the result of the convolution of the coherence function envelope and the sum of "DC terms", interference between light waves returning from reference and sample arms, and the interference between light waves from different reflectors in sample arm. All the terms are in spatial domain as a function of axial position *z*. When the power from reference arm is great enough compared to the power of sample arm, the ratio I_s^2/I_r^2 is safe to be negligible and the auto-correlation artifacts can be reduced. Therefore, SD-OCT systems are allowed to run at high acquisition rate.

Section 1.3 Multi-functional OCT visualization

Figure 1.4 is the schematic of the SD-OCT system used in all the experiments presented in this thesis content. It is a GPU-accelerated real-time polarization-sensitive SD-OCT with broadband infrared laser light source at center wavelength of 1310 nm (1310 SD-OCT system). [5] Light from two super-luminescent diodes (SLD) source passes through a polarization beam splitter (pbs) and a polarization modulator (pm) in the source arm. Although polarization-sensitive imaging is one of the most important extension functions of this SD-OCT system which provides birefringence information of sample, the principle of polarization-sensitive OCT imaging will not be discussed in this thesis report.

The source light is sent to a fiber circulator, which controls the travel direction of optical signals to prevent reflected light entering source arm fiber, and then a 90/10 beam splitter (bs), which splits source light unevenly as 90% of total power goes into sample arm while 10% goes into reference arm. In sample arm, two perpendicular mirrors operated by galvanometer control transverse scanning. A replaceable lens with 30 mm focal length (not shown on the figure) is mounted on sample arm handpiece to make scanning light beam focused on a region approximately 10 μm in diameter. There is a neutral density filter (ndf) placed in reference arm to adjust the power of light reflected from reference mirror. The reference mirror remains stationary during imaging, but its position can be manually adjusted upon the need of depth focus interest in sample sub-surface region. Backscattered light from both arms recombines at the beam splitter and this is where the interference happens.

In detection arm, coherent light with depth information is collimated by a collimator (c) in the end of optical fiber and sent to a transmission diffraction grating. The diffraction grating splits light in to an array of spectrum. This spectrum is in Fourier domain as a function of wavenumber. Since the spectrum beam is dispersed, a planoconvex lens is mounted to focus the light of spectrum on the charge-coupled device (CCD) array of line scan cameras (lsc). A polarization beam splitter (pbs) cube separates the power of spectrum and distributes the spectra with different polarization states to two line scanning cameras in the end of detection arm. One camera is placed straight along the direction of light propagation (straight camera) whereas the other is placed vertically to the original beam

path on the side (side camera). Two cameras being employed in this SD-OCT system is for polarization-sensitive imaging purpose.

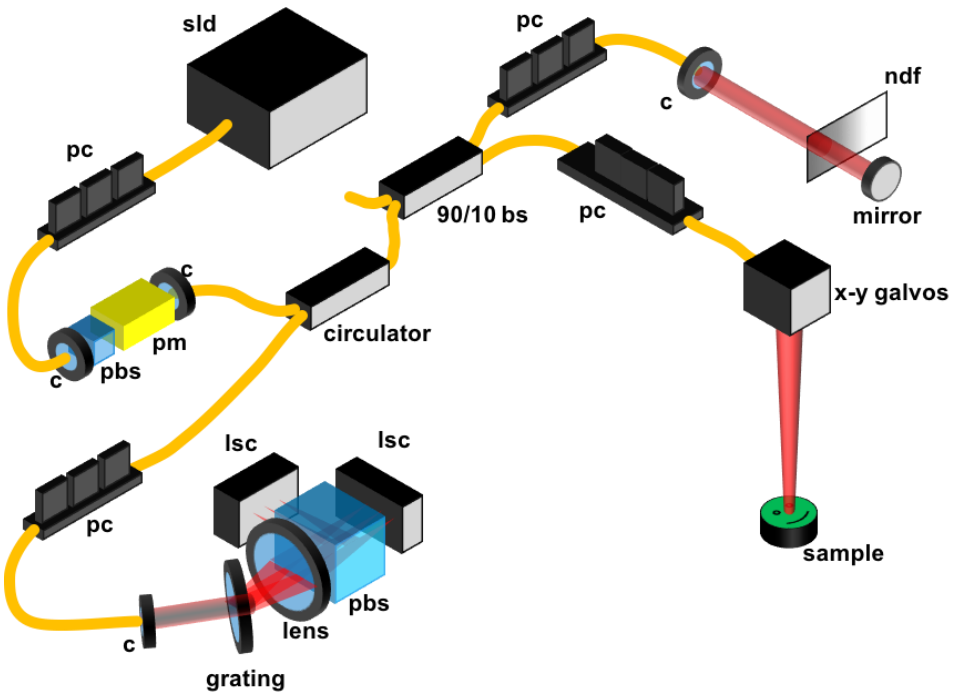

Figure 1.4 Schematic of GPU-accelerated real-time polarization-sensitive SD-OCT that has been used for experiments in this thesis. The center wavelength of light source is 1310 nm. sld: super-luminescent diodes; pc: polarization controller c: collimator; pbs: polarization beam splitter; pm: polarization modulator; bs: beam splitter; ndf: neutral density filter; lsc: line scan camera

During OCT scanning, the cameras open and close an integration window to expose light spectrum on the CCD arrays. The optical signal is converted to electrical signal and processed by a GPU-accelerated computer according to the procedure described in equations Eq. 1.6 ~ Eq. 1.9. Thus the sub-surface depth-resolved information of a specific tiny region is obtained. This information is expressed as a function of reflection intensity versus depth, which is called depth profile or A-line. Each A-line has 512 pixels

corresponding to approximately 2 mm in physical depth. The galvanometers sweep the incident light across the sample by controlling the angle of the mirrors inside, so that two-dimensional (2D) cross-sectional image (frame) and three-dimensional (3D) volume can be formed. In following chapters of this thesis, one single frame is composed of 2048 A-lines as default unless specified, while the frame number of a volume is subject to experiment setting.

Chapter 2 OCT system optimization and sensitivity check

Section 2.1 Spectrometer in SD-OCT and aim of system optimization

Broad-band interference light with axial information is detected by OCT camera in spectrum form as a function of wavenumber k (k-space). This dispersed spectrum is obtained by an optical spectrometer when light travels through dense tiny slits of a transmission diffraction grating. Each point on the incident light wave front that propagates through a slit becomes an individual point source. Since each point source has the same power and phase features, the emitted light waves interfere with each other and the enhanced wave with specific frequencies present a rainbow-like spectrum pattern (Figure 2.1).

In Figure 2.1, the collimated incident light hits the diffraction grating with a normal-incident angle of θ_i, and the emitted angle θ_m is a function of wavelength. This relationship is described mathematically in Eq. 2.1 and Eq. 2.2.

$$d(\sin\theta_i - \sin\theta_m) = m\lambda \qquad \text{Eq. 2.1}$$

$$\theta_m(k) = \sin^{-1}\left(\sin\theta_i - \frac{2\pi m}{kd}\right) \qquad \text{Eq. 2.2}$$

In Eq. 2.1 and Eq. 2.2, d is the spacing between two slits, λ is the wavelength, and $k = 2\pi/\lambda$ is wavenumber. The order of diffraction is denoted as m. When the wave travels

through a transmission diffraction grating, most of the power continues propagating the original direction. This portion of direct transmission light is called 0^{th} order ($m = 0$). And the second maximal power, denoted as 1^{st} order ($m = 1$), occurs next to 0^{th} order with an angle θ_1. And the plot in Figure 2.1 (b) indicates a non-linear relationship between the dispersion angle of 1^{st} order light of the diffraction grating (Wasatch Photonics, HD 1145 l/mm @ 1310 nm, Logan, Utah, USA) that is used in 1310 SD-OCT system.

The 1^{st} order of light is the spectrum received by SD-OCT camera. A lens is mounted to focus the spectrum on the CCD array with thousands of photo-sensitive elements in line scanning camera. Each of the element only receives light from specific wave number that corresponds to one pixel on spectrum distribution in *k*-space. However, according to Eq. 2.2 and considering the angle change of beam due to the lens, the spectrum is not evenly distributed on CCD array. [6] This uneven spectrum spacing in *k*-space will cause difficulty for computer to construct depth profile by performing inverse Fourier transform properly. [6], [7] Therefore, we must determine the exact wavelength (wavenumber) received on each pixel and calibrate the spectrum in a linear distribution form.

In practical situation, the optical components including the grating, lens, polarization beam splitter and cameras are mounted on adjustable stages on a piece of optical bread board. The configuration of the detection arm can slightly change over time due to various factors such as mechanical deformation, continuous adjustment for various experiments and false operation by user. Since the whole detection arm is sensitive to its configuration

setup, even tiny off-focus on CCD array results in the necessity of re-calibration as well as significant signal-to-noise ratio (SNR) and sensitivity decrease.

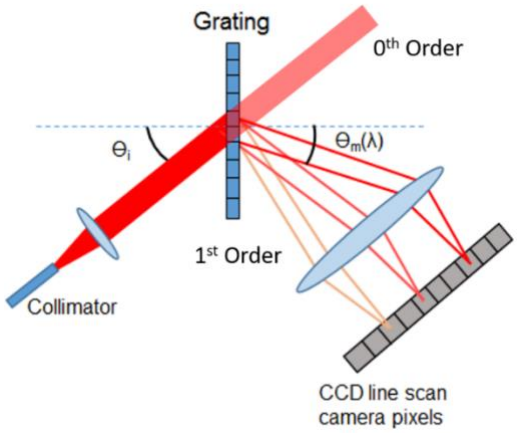

(a)

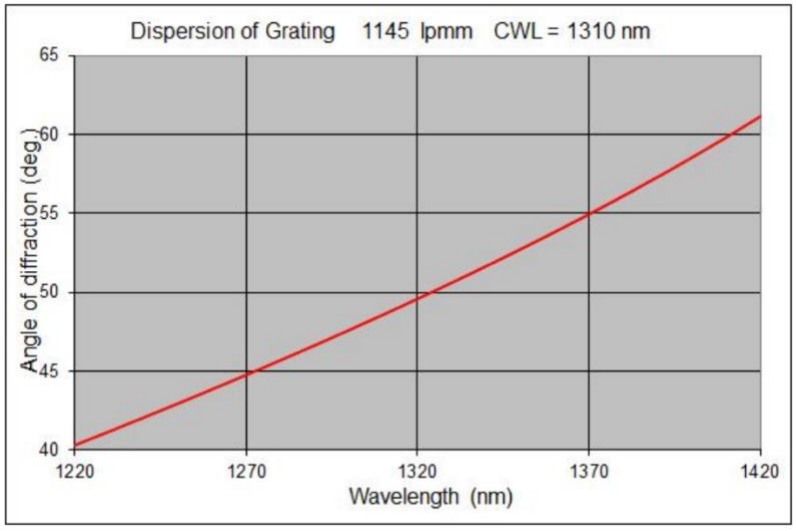

(b)

Figure 2.1 (a) The transmission diffraction grating-based spectrometer in 1310 SD-OCT system. Incident light is collimated by a collimator and most of the power continues its propagation in the same direction after passing through the grating (0th order). 1st order light beam is the dispersed spectrum in *k*-space. The spectrum is focused on the CCD array of line scanning camera. (b) Dispersion feature of the grating used in 1310 SD-OCT system (Wasatch Photonics, HD 1145 l/mm @ 1310 nm, Logan, Utah, USA). It is expressed as a non-linear curve of angle of diffraction versus wavelength.

The aim of system optimization is to raise system sensitivity for better image quality. This chapter will be focusing on the alignment of optical components in detection arm and wave number calibration in data processing as attempts to increase system SNR and sensitivity.

Section 2.2 System optical power measurement

1310 SD-OCT system is a fiber-based system which makes it possible to measure the optical power of each part in the system by connecting fiber end to an optical power meter (Newport, Power Meter 1918-C) with a measurement head covers wavelengths centered at 1310 nm. Due to the power loss either from the connection nodes or spicing regions in the system, we need to ensure the output optical power in the detection arm is still high enough to be measured. A detailed schematic of 1310 SD-OCT system is shown in Figure 2.2. Before measurement, the power output from SLD laser source needs to be maximized by twisting the source fiber via the polarization controller in source arm. And the power output from the fiber ends in other parts of the system is required to be maximized by adjusting the corresponding polarization controller as well.

The results of measurement are labeled in Figure 2.2. In order to reduce the power loss, we reduced the number of bulkheads and replaced old spiced fibers with new short fibers. The total output received from source arm is 12.02 mW and 9.56 mW of the total is sent to the 90/10 beam splitter. The ratio of the power detected from sample arm fiber to that from reference arm fiber is close to 90/10 beam splitting property. During detection

arm power measurement, a mirror is placed on the focal plane of objective lens in the end of sample arm. The mirror is adjusted to maximize the power of returning light from sample arm. Because light passes through the beam splitter again, only 90% of returning coherent light from both sample and reference arm enters the detection arm. The maximum of output from fiber in detection arm is 3.20 mW. The power measurement ensures that each optical component in the system is working properly and signal output is strong enough for cameras. The system optimization process is thus the optimization of detection arm.

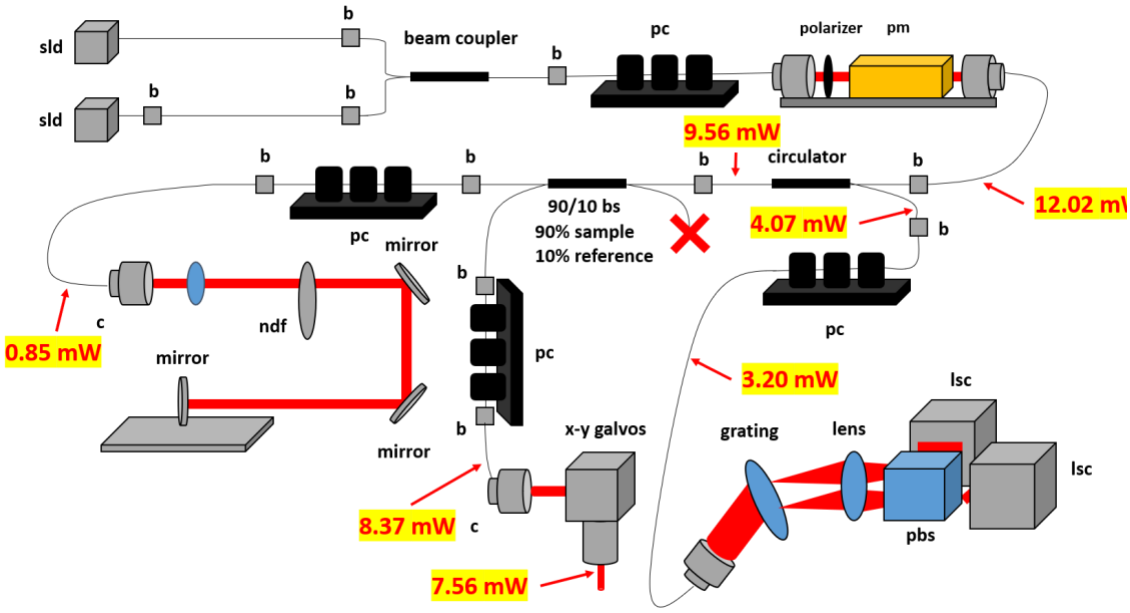

Figure 2.2 Detailed schematic of 1310 SD-OCT system with power measurement labeled next to corresponding nodes. sld: super-luminescent diodes; b: bulkhead; pc: polarization controller c: collimator; pbs: polarization beam splitter; pm: polarization modulator; bs: beam splitter; ndf: neutral density filter; lsc: line scanning camera

Section 2.3 Detection arm alignment

Section 2.3.1 Diffraction grating incident angle

The CCD array on SD-OCT camera receives power of 1st order diffracted light from spectrometer. In order to raise the power of signal, this portion of power is desired to be maximum. The division of optical power after light passes through a diffraction grating can be quantitatively described by diffraction efficiency. The diffraction efficiency of a given diffracted order m is defined as the diffracted power divided by incident power, and is a function of incident angle θ_i. However, theoretically the diffracted light ($m \neq 0$) is dispersed and has infinite width, which makes accurate direct power measurement difficult. According to a review by Gaylord and Moharam [8], the diffraction efficiencies of 0th order and 1st order are significantly greater than other orders. This means most of the power propagates along undiffracted light beam and 1st order spectrum. This feature provides us a much feasible approach to roughly determine the maximum of 1st order by finding the minimal power of undiffracted 0th order light beam, since the latter is collimated and easy to measure by optical power meter.

We mounted the diffraction grating on a rotational stage so that the incident angle can be adjusted (Figure 2.3). The propagation direction of 0th order light does not change as rotating the grating according to Eq. 2.2. Therefore, the power meter detection head can be fixed in a small range of positions to compensate the beam transverse displacement due to refraction. Once the minimum of 0th order power is reached, the incident angle is

determined. Then the beam path of 1st order can be found by multiple power measurement on the side of undiffracted beam path.

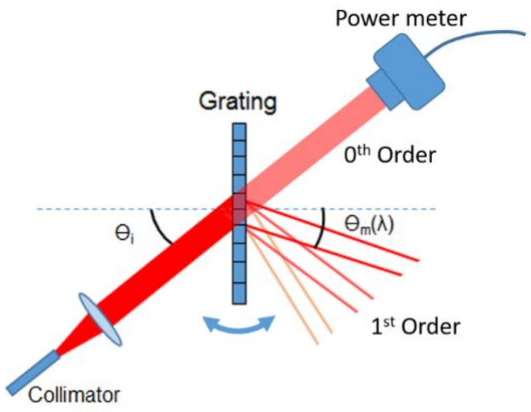

Figure 2.3 The method to determine the maximal power of 1st order spectrum by rotating grating. As the undiffracted 0th order beam stays the same propagation direction, a power meter is mounted to measure the power of 0th order light. Maximal 1st order can be roughly found when 0th order beam reaches its minimal power.

Section 2.3.2 Line scanning cameras alignment

The track of beam path provides reference lines for subsequent positioning of focus lens, polarization beam splitter and cameras. These components can then be placed properly as shown in the schematic in Figure 2.4 (a). The most important step is the placement and alignment of cameras. Maximal signal power can only be received when the spectrum is focused exactly on camera CCD array. Moreover, since two line scanning cameras are employed in 1310 SD-OCT system for polarization data purpose and the spectrum is split by a cubic polarization beam splitter, the pattern of spectra received on the two cameras has to be nearly identical. This requires fine position tuning to both cameras.

The system acquisition program displays spectra patterns (Figure 2.4 (c)) during scanning. The value of spectrum sum indicates the total power received by both cameras. Before starting alignment, we blocked the reflected light from sample arm because we need to eliminate the interference from environment under sample arm and maintain stable detection input. We placed the first camera on focal plane of straight beam and roughly adjusted the position. When there was signal detected by camera, we used polarization controller to shift all power to this straight camera. A round continuously variable neutral density filter is added in between collimator and grating to avoid power to be saturated in spectrum window. The camera was then fine-tuned by screwing micro-controlling knobs on camera stage to reach the maximum spectrum sum (Figure 2.4 (d)). After finishing the straight camera, we shifted all power to side beam and repeated the same process to mount the side camera. Additional fine tuning is necessary when the two spectra do not match well when the polarization power is equally assigned to the cameras.

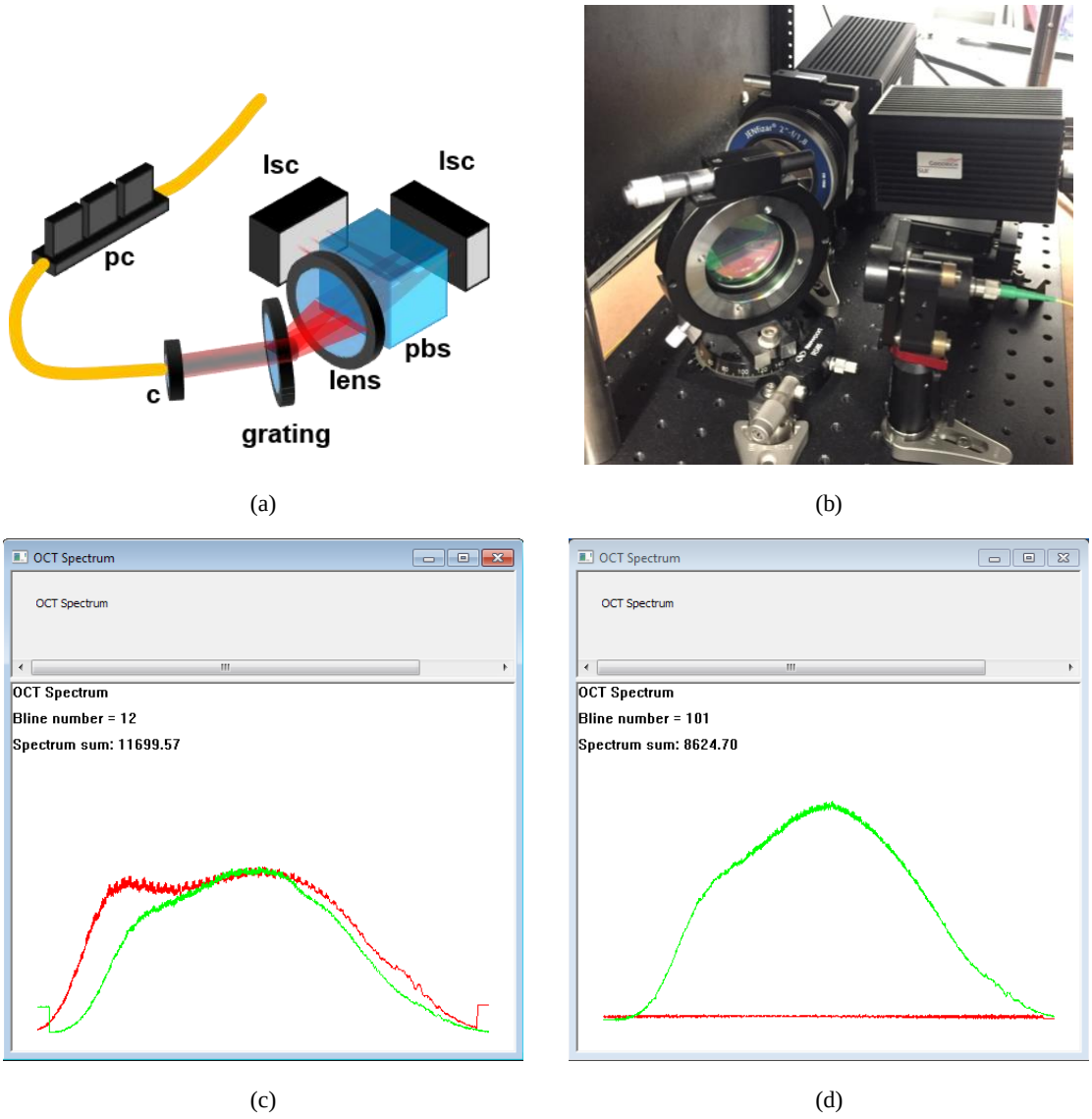

Figure 2.4 (a) Schematic of detection arm. A cubic polarization beam splitter is placed in between the focus lens and two line scanning cameras to split light with different polarization states. The CCD arrays in the cameras have to be placed exactly on the focal plane and aligned with each other. (b) A photo of detection arm. The grating is mounted on a rotational optical stage. (c) In optimal condition, the spectra displayed by acquisition program should be aligned and in high spectrum sum. The spectrum received from straight camera is represented by the green curve while the spectrum from side camera is represented by the red curve. (d) The power of spectra is shifted to one camera (straight) by adjusting polarization controller (pc in (a)) during the corresponding camera alignment.

Section 2.4 Wavelength calibration

Section 2.4.1 Wavelength calibration setup

Previous study from Wojtkowski [9] and Mujat **Error! Reference source not found.** has revealed the importance of wavelength calibration in proper depth profile conversion for SD-OCT imaging. The mapping of wavelength distribution can be optimized by measuring a reflective sample surface. Eq. 1.5 and Eq. 1.6 present that the cross-correlation portion in current intensity that contains axial information is modulated in a form of cosine wave. This sinusoidal modulation indicates that ideally, the high-reflective surface at certain depth plane only corresponds to one single modulation, where higher frequency modulations corresponds to deeper reflectors. This relationship can be expressed in Figure 2.5. The power of reflection can be found by the magnitude of fringes in *k*-domain or height of peak in spatial domain. Most power is reflected from the reflective surface where there is a sharp high peak in depth profile.

Because of the uneven mapping of wavelength, the initial spectrum received on CCD array contains modulations with a range of frequencies rather than a perfect sinusoidal modulation. The peak in depth profile is then broader that leads to blurred images and low SNR. Therefore, proper calibration of wavelength is critical in SD-OCT raw data processing.

We placed a mirror on the focal plane of objective lens as high-reflective surface. Two variable neutral density filters were inserted to reference and sample arms, respectively, to

adjust the returning power from both arms. The beams from two arms were adjusted to the sample power level for better coherence pattern (Figure 2.6). The galvanometers were set to 0V since lateral scanning is not required and the noise from galvanometer mirror rotation. A few frames of A-lines were recorded for data processing.

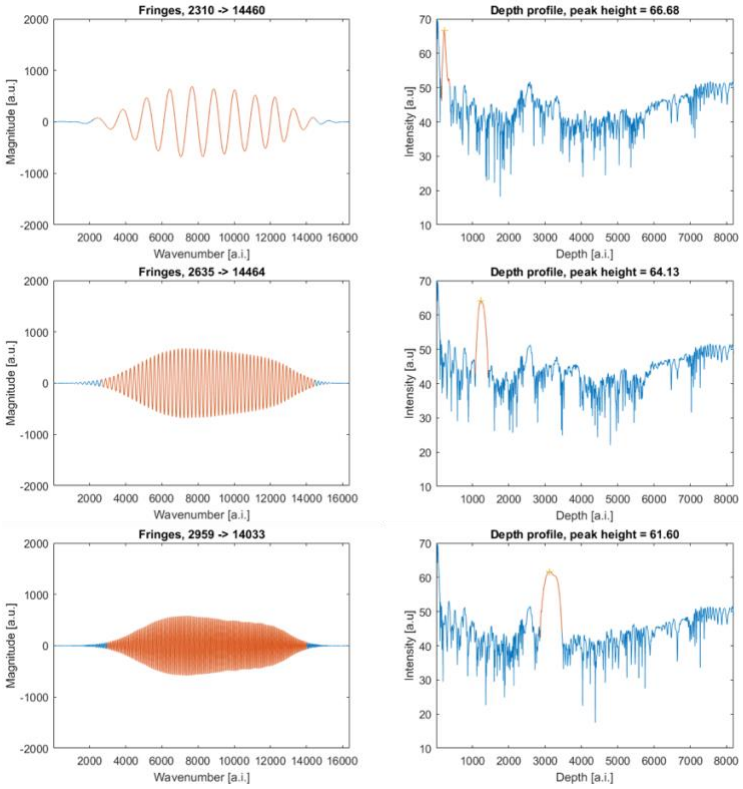

Figure 2.5 The relationship between sinusoidal modulation in *k*-space and reflector depth in spatial domain. Higher frequency modulation corresponds to deeper reflector. The intensity of spectra modulation or the peak height in spatial domain indicates the power received at corresponding axial positon (or the reflectivity of the reflector).

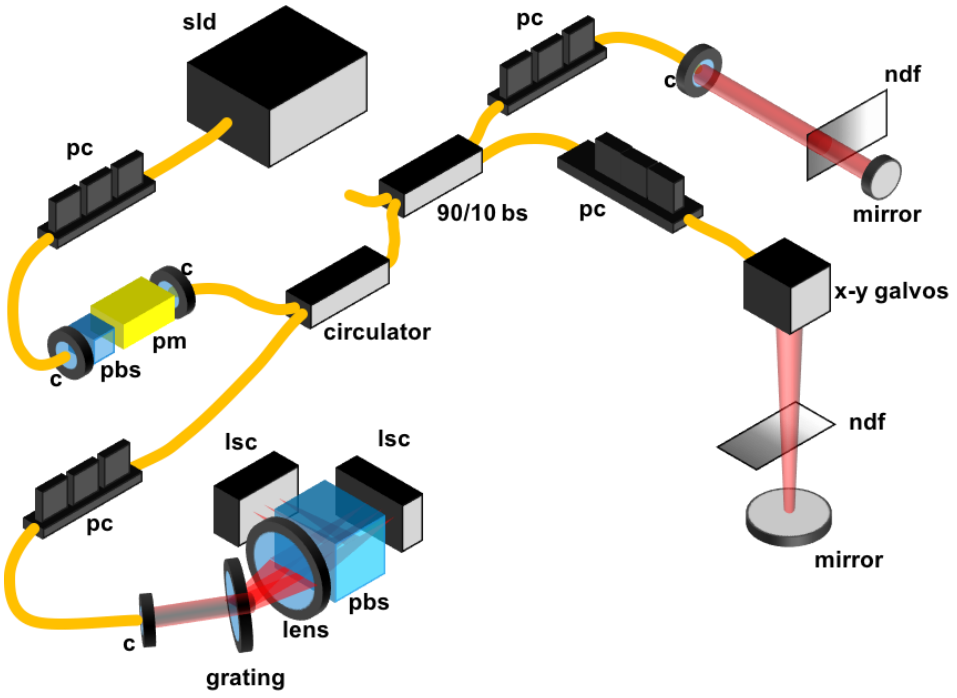

Figure 2.6 Schematic of calibration data taking. A high reflective surface (mirror) is placed on the objective focal plane and a neutral density filter is inserted in sample arm to adjust sample power. This schematic also applies to system sensitivity check in Section 2.5. sld: super-luminescent diodes; pc: polarization controller c: collimator; pbs: polarization beam splitter; pm: polarization modulator; bs: beam splitter; ndf: neutral density filter; lsc: line scanning camera

Section 2.4.2 Calibration data processing

The reflective sample data was processed based on an iterative autocalibration technique reported by Mujat [6] in MATLAB computing environment (MathWorks, R2016b). This technique assigns wavelength based on the linearity of the phase of perfect sinusoidal modulation. An array of corrected wavelength distribution is saved for future actual data processing. This method overcomes the limitation of previous calibration techniques that separate wavelength measurements are required for different imaging. [9]

The mean of intensity modulation of the spectra in *k*-space of 2048 A-lines in a frame is shown in Figure 2.7 (A1, B1). This spectrum is the visualization of features governed by Eq. 1.6. Reflective surface reduces the interference fringes resulting from sample structure. Both edges were cleaned and made to converge to zero to reduce systematical errors. The spatial information is obtained by performing Fourier transform as illustrated in Figure 2.7 (A2, B2). The peak represents the axial position of mirror which is a form of spectrum in Fourier domain. A bandpass filter (orange region in Figure 2.7 (A2, B2)) is applied in Fourier domain so that the interference fringes are isolated and DC term is removed [6] as shown in Figure 2.7 (A3, B3). The ideal fringes pattern should be perfect periodic sinusoid as a function of wavenumber *k,* and thus the phase is linear.

Figures in Figure 2.7 Column A are an example of initial spectrum without wavelength calibration. The peak in spatial domain (Figure 2.7 (A2)), is broad in width which indicates the detected spectrum is a result of the summation of a wide range of multiple frequencies due to the unevenly *k*-space distribution. The phase of interference fringes presents non-linearity as shown in blue curve in Figure 2.7 (A4) compared to the perfect linear black line. This black line is an optimal estimation of the phase from proper wavelength assignment. The proper wavelength array can be generated based on the geometrical design of spectrometer or third order polynomial that brings the generated wavelengths in spectral range of the light source.[6], [10] The goal in the calibration iteration process is to force the phase lines to overlap so that the wavenumbers on *x*-axis are re-assigned as a function of array index. In this process, the peak in Fourier domain is

sharpened so that the sinusoidal modulation is refined. In the phase linearization, the wavenumber k on actual measurement curve (blue) corresponding to certain phase value is shifted to the wavenumber k_{ref} on reference curve (red) that corresponds to the same phase. The spectral interference fringes are interpolated by the new calibrated wavenumber array and zero-padding is applied to improve the quality of interpolation. [6]

We repeated the procedure in multiple iterations because the phase curve could not be perfectly aligned with reference curve in one operation. Corrected wavenumber array was used as initial array in the next iteration. Error was analyzed by measuring the offset of nonlinear part to its polynomial fit and error level is defined by the sum of maximal offset on both sides of the polynomial fit curve. The iteration stopped when the error level reached a number smaller than a preset threshold. The figures shown in Figure 2.7 Column B is the result after 1369 iterations. The error level in Figure 2.7 (B4) drops from 21.1005 to 0.0035 (values are in arbitrary unit) which means the calibrated phase curve is well aligned with the reference curve. The peak in Fourier domain converges into a sharp peak and peak height rises from 65.35 to 70.73 (Figure 2.7 (B2), values are in arbitrary unit). The interference fringes pattern in Figure 2.7 (B3) shows clear identical periodic pattern compared to those in Figure 2.7 (A3). The corrected wavelength array is saved and can be used in future data of biological sample processing. In conclusion, this auto-calibration method is effective in wavelength distribution correction and simplifies SD-OCT imaging processing. To evaluate the quality of calibration, system sensitivity needs to be determined.

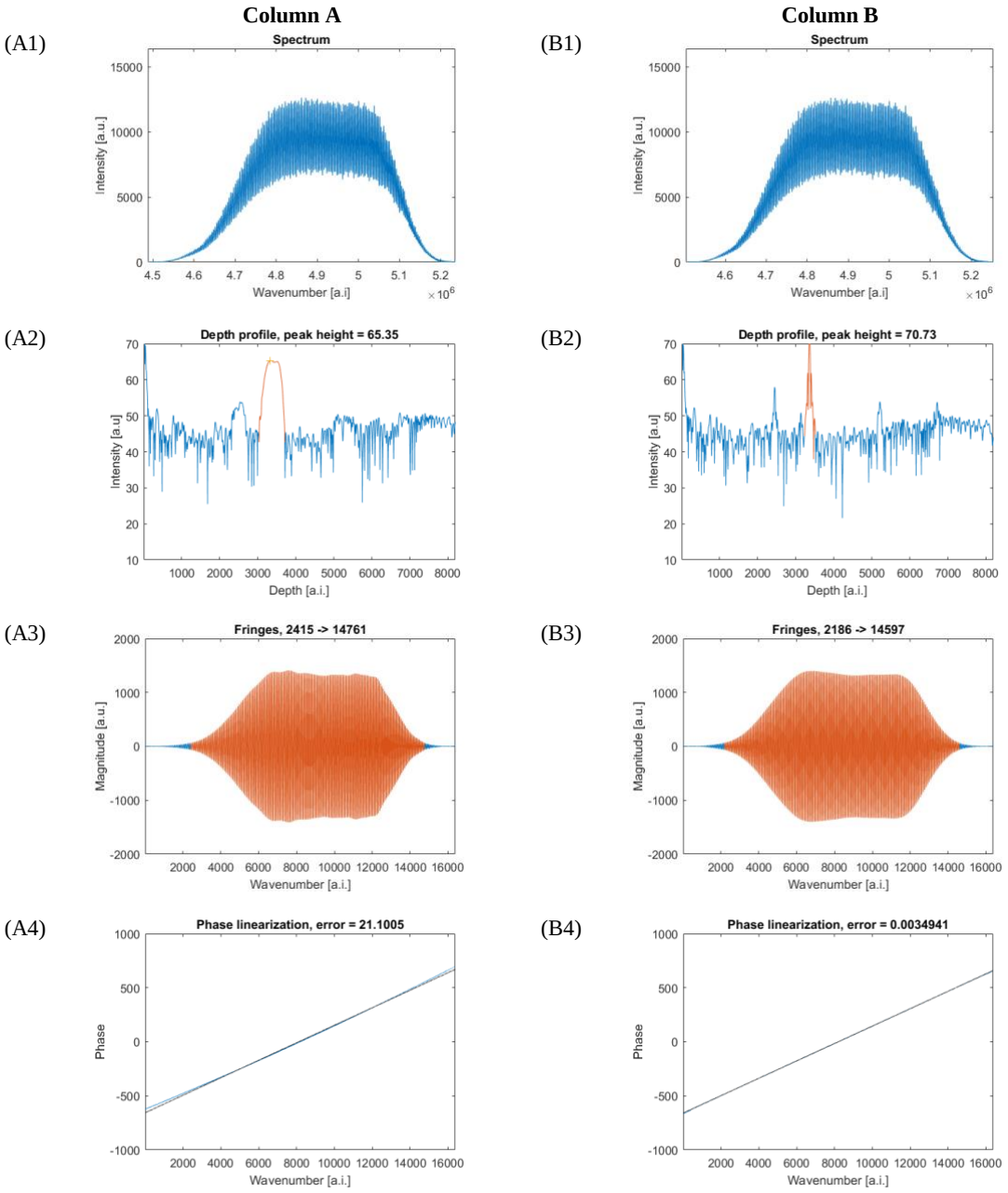

Figure 2.7 Comparison of various parameters measurement before (Column A) and after (Column B) wavelength calibration. (A1) and (B1) are spectra (in arbitrary unit [a.u.]) as a function of wavenumber (in wavenumber array index [a.i.]) received by one camera. (A2) and (B2) are depth profiles, which are also the spectra in their Fourier domain. The intensity and axial position of mirror is the orange portion. The initial peak in (A2) is broader than the calibrated peak in (B2) because there are multiple modulations in initial peak due to the unevenly distribution of wavenumber. (A3) and (B3) are spectral interference fringes as output of spectra after a bandpass filter. The interference fringes in (B3) shows identical periodic pattern after calibration. (A4) and (B4) are the phase curves from interference fringes (in blue) and reference linear phase curve (in black). The lines in (A4) are not aligned well especially near the start and end points. During calibration iterations, the blue phase curve was generally shifted to the reference black curve and linearized. As shown in (B4), the phase curve overlaps the reference well. The error level converges.

Section 2.5 System sensitivity measurement

Section 2.5.1 System sensitivity measurement setup

System sensitivity represents the ability of an SD-OCT to identify sample structures in image when the change of optical input is small. It is defined as the ratio of maximum signal over noise floor. [2] The maximum signal is obtained by placing a perfect reflector in the sample arm. [12]

The system setup is similar to wavelength calibration setting in Figure 2.6. The power from reference arm is set to be high enough for actual imaging. Since 90% of total power is sent to sample arm, if a mirror is placed on the focal plane as sample, the returning power must be reduced to avoid saturation in spectrum. So we placed two neutral density filters with 20 dB attenuation each. Thus the total attenuation from sample arm is 80 dB because of the double-pass nature of light detection. During data acquisition and processing, new wavelength calibration is applied.

Section 2.5.2 Results

System sensitivity is calculated from depth profile of the mirror image. Depth profile illustrate the intensity in spatial domain as a function of depth. The intensity in depth profile is in decibel scale and sensitivity can be calculated simply by the difference between peak and noise floor. The attenuation when light travels through neutral density filters should also be considered in total sensitivity determination. The results shown in Figure 2.8 are mirror images and mean depth profiles from straight camera, side camera and combined

processing of data from both cameras. Noise level is obtained from the mean of noise floor near the peak as labeled in red. The measurement indicates that straight camera has sensitivity of 94.37 dB while side camera has 100.28 dB. The overall sensitivity of the combination of straight and side camera is 98.25 dB. The system sensitivity should consider the combined result from because typically in post processing, the SD-OCT images are obtained from equal contributions from both cameras. The system sensitivity measurement result shows that the detection arm was built well, and wavelength calibration is good enough for the system to obtain high SNR in biological sample imaging.

Then we tested the image quality by using finger as biological sample. We performed 2D scanning in a range of 2 mm on finger. Details of structural information, such as ridges, epidermis and partial dermis can be clearly identified from the images shown in Figure 2.9. The SNR was calculated in a similar way by subtracting noise floor from surface peak. The measured SNR in combined image was 39.68 dB, which is enough for good image quality. [17] Additionally, the SNR of subsurface region received by side camera is higher than that of straight camera. The side camera has better working condition.

(a)

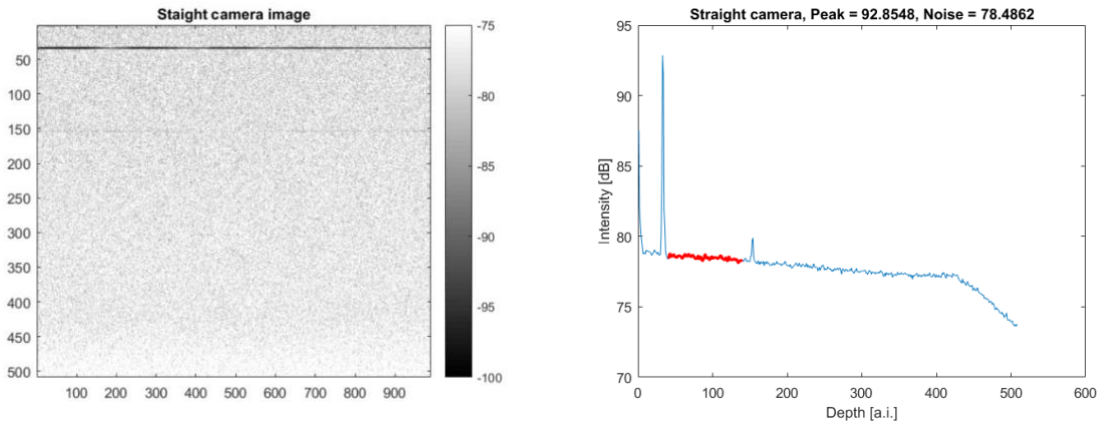

(b)

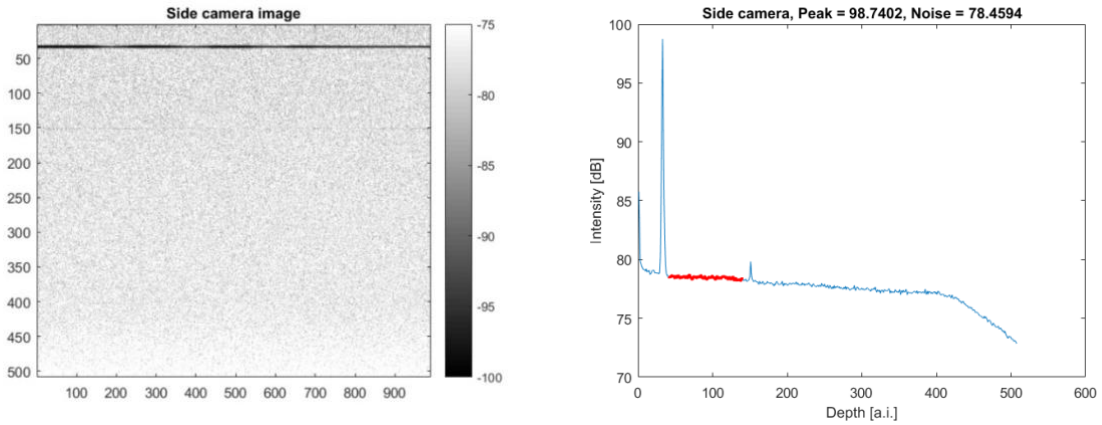

(c)

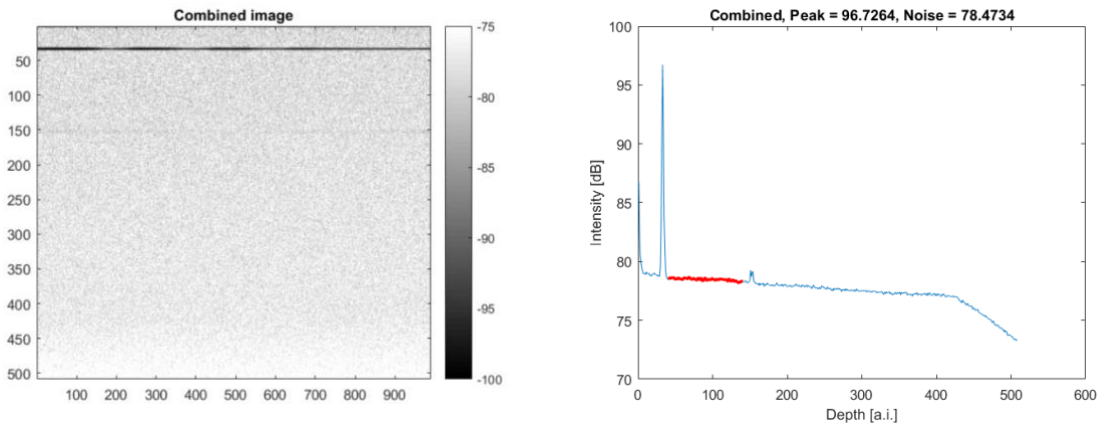

Figure 2.8 The result of system sensitivity check from straight camera (a), side camera (b) and the combination of both cameras (c). The mirror surface is shown as the line in left intensity images and as the peak in right depth profiles. Noise level is obtained by calculating the mean of noise floor labeled in red portion.

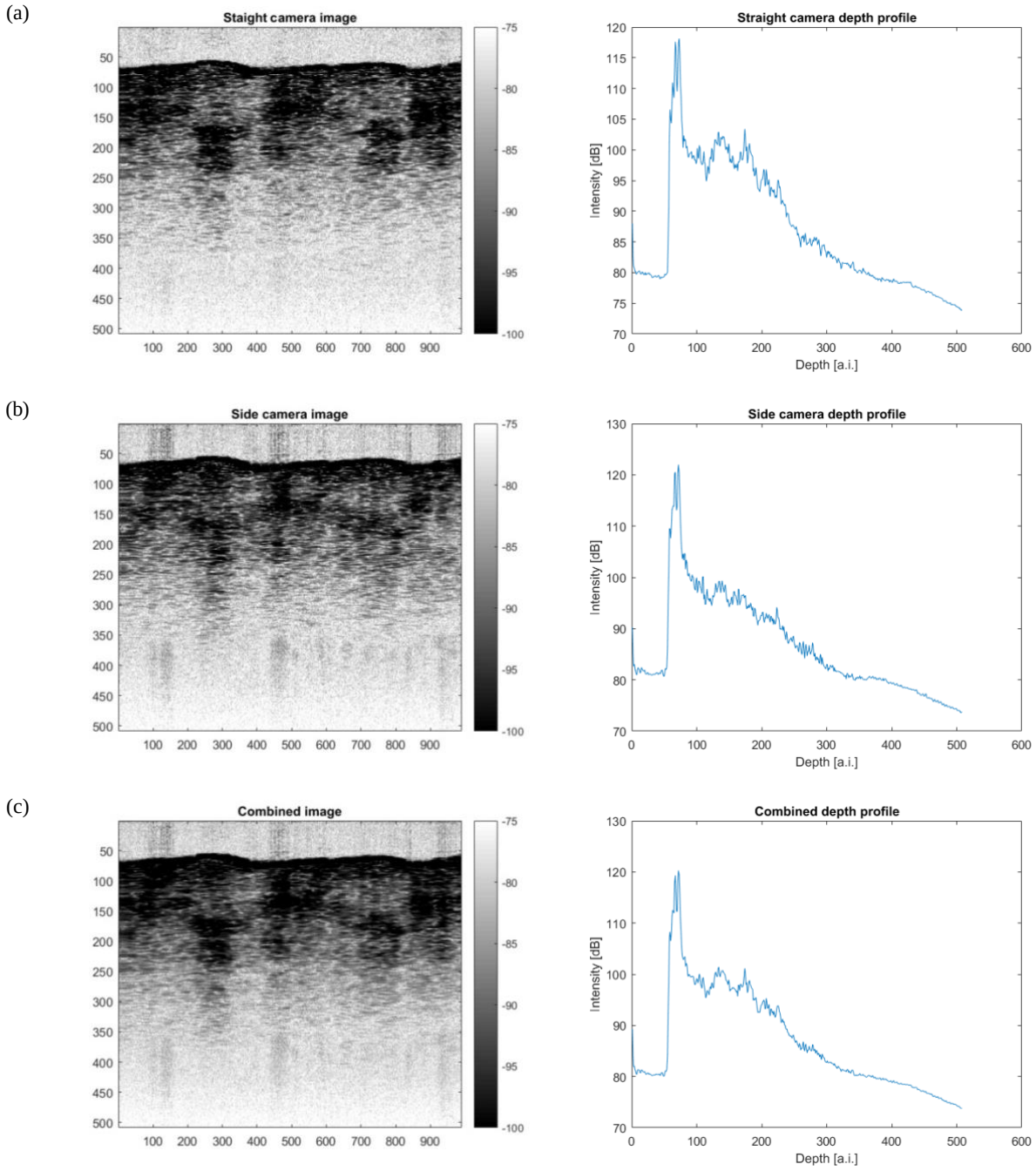

Figure 2.9 System SNR check on biological sample. The images were captured from a line of approximately 2 mm on finger. The images on left side show clear sub-surface identity. Epidermis and part of dermis can be seen. The SNR from each camera can be calculated from corresponding depth profiles.

Chapter 3 Three-dimensional cerebral cortex OCT image registration

Section 3.1 Introduction

Section 3.1.1 Information extracted from SD-OCT image

1310 SD-OCT system is a multi-functional system that is capable for fast real-time 3D scanning. After the system optimization in Chapter 2, the system is able to run at maximal acquisition rate (A-line scanning rate) of 30 kHz, which is 14.65 frames per second. We used 16.5 kHz (8.06 frames per second) for less time-rigid brain scanning experiments that has been introduced in Chapter 3 and Chapter 4 for better SNR and optical characterization.

3D volumetric images can be constructed due to the fast scanning speed. Generally speaking, a 3D volume is composed of 100 or 200 consecutive cross-sectional frames and visualized by MATLAB or some 3D visualization software such as Amira and Avizo (FEI Visualization Sciences Group, Bordeaux, France). Figure 3.1 shows the steps in the construction of a 3D volumetric image.

Multiple optical features of tissue sample can be obtained by performing various methods in data processing including intensity, attenuation and flow. Birefringence information can also be analyzed from different polarization states received by two cameras. [5], [13]

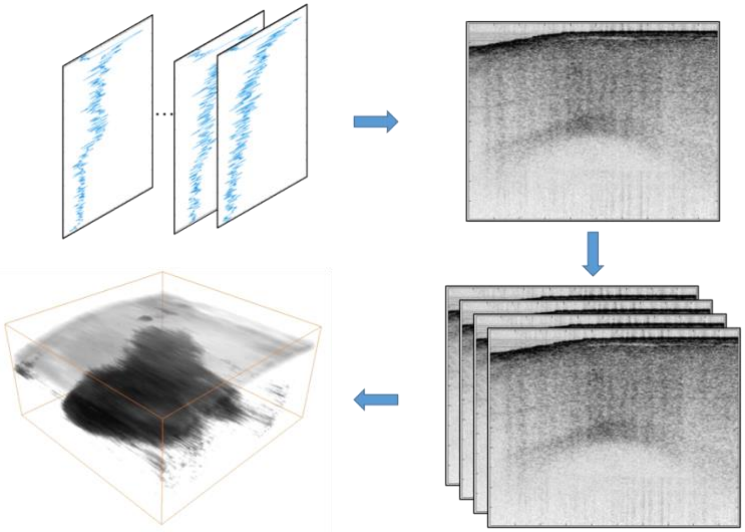

Figure 3.1 The general process of 3D volumetric OCT image construction. 2D cross-section intensity image is obtained by multiple depth profiles when laser light beam scans across sample. Successive frames placed in proper order create a 3D volumetric image with the aid of 3D visualization software.

Intensity

The most frequently-used image modality is intensity image. It is formed by combining multiple depth profiles inverse Fourier transformed from spectrum. Intensity images represent the intensity of photo-current or the returning power from reflectors along axial direction. The inverse Fourier transform in Eq. 1.6 ~ Eq. 1.9 yields complex depth profiles. These depth profiles are denoted as $H_n(z_m)$ and $V_n(z_m)$ for straight and side camera, respectively. Combined intensity contributed from both cameras can be computed according to Eq. 3.1. [12]

$$I_n(z_m) = H_n(z_m) \cdot H_n^*(z_m) + V_n(z_m) \cdot V_n^*(z_m) \qquad \text{Eq. 3.1}$$

where * represents the complex conjugate. Intensity images are displayed in logarithmic scale.

Attenuation coefficient

In SD-OCT scanning, the power of coherent light in biological tissue is attenuated along axial propagation because of the scattering and absorption from medium. In homogenous medium, the attenuation of light power can be expressed in Lambert-Beer's Law (Eq. 3.2)

$$L(z) = L_0 e^{-\mu z} \qquad \text{Eq. 3.2}$$

where $L(z)$ is the irradiance (power per unit area) after beam propagating a distance z. $L_0(z)$ is the initial irradiance of incident light while μ is attenuation coefficient. Attenuation coefficient is dependent on the optical nature of medium, and according to Eq. 3.2, greater attenuation coefficient leads to higher ability in light scattering and absorption of a certain medium.

OCT system sends light with constant power into biological sample. It is common that there is insufficient power reaching the reflectors below a high light-scattering or absorption subsurface layer. Therefore, the intensity from such reflectors does not represent the exact optical properties. A reconstructed image of the mapping of attenuation coefficients has been proved to be an effective way to overcome this limitation. [14] In SD-OCT images, the relationship between attenuation coefficient and intensity can be expressed as

$$\mu(z) = \frac{I(z)}{2\int_z^{\infty} I(u)\mathrm{d}u} \approx \frac{I(z)}{2\int_z^{D} I(u)\mathrm{d}u} \qquad \text{Eq. 3.3}$$

where D is the depth range of SD-OCT system.

Flow

Flow images represent the phase difference between two successive positions in sample. During OCT imaging, sample motion causes phase change due to Doppler effects. Based on complex depth profiles after Fourier transforming from spectrum, two types of flow information can be obtained, bi-directional and phase variance. [5], [13] Bi-directional flow is the weighted phase difference of two successive depth profiles at corresponding depth, whereas phase variance is the weighted square of this phase difference.

Flow images are commonly used in blood flow detection in *in vivo* OCT image. The angle of the phase at each pixel can be measured by calculating Fourier transform of the intensity A-lines. And since Doppler effect happens on contiguous A-lines, the flow image is then obtained and the values of indices on flow images show a relative velocity of blood flow.

An example of intensity image, attenuation coefficient image and flow image of a mature mouse brain cortex and corpus callosum region is shown in Figure 3.2. 3D volume of the mapping of attenuation coefficient and blood flow pattern from the whole brain can be visualized in Figure 3.3.

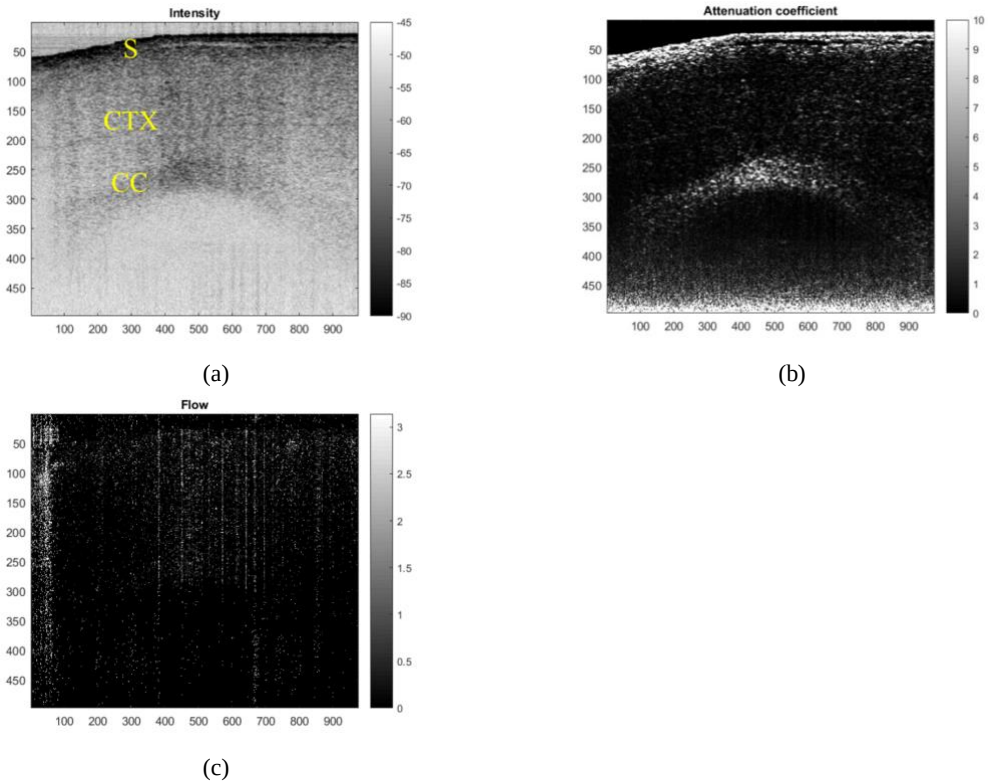

(a) (b)

(c)

Figure 3.2 An example of the three types of image introduced in Section 3.1.1. (a) Intensity; (b) attenuation coefficient, (c) flow. Images are a cross-sectional frame of mouse cortex. S: cortex surface; CTX: cortex; CC: corpus callosum.

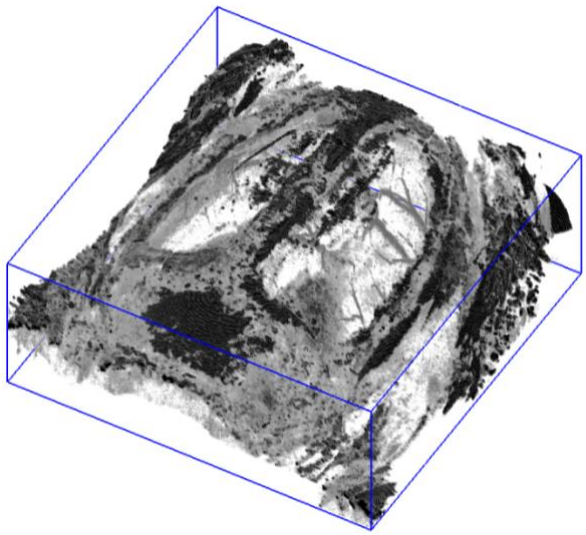

Figure 3.3 An example of 3D volumetric image of mouse brain constructed from the combination of attenuation coefficient and flow images. Structural information, such as cortex, corpus callosum and cerebral vessels, is visualized. This volume is processed and created by MATLAB.

Section 3.1.2 Purpose

Various current collaborating research projects that are assisted by this 1310 SD-OCT system require multiple imaging on the same sample region at different time points. The research teams intend to track specific changes in biological tissue optical properties over time. Determination of the same scanning regions in various scanning is crucial in order to control irrelevant variables. Looking for the same region manually by placing the sample at the exact same position as previous time points is difficult. In addition, the growth of subject animal also induces structural difference on sample surface.

A fast image registration method to align regions of interest in 3D volumetric level is introduced in this chapter. Two volumes of mouse cortex data from initial time point (Day 0) and 30-day time point (Day X) are taken as post-processing example. The procedure of 3D alignment contains two stages, *en face* image transverse registration and optical parameter axial alignment. Flow images were used for transverse registration since it maps cortex blood vessel pattern, while attenuation coefficient images were used for axial alignment because attenuation coefficients are not greatly influenced by low SNR in deep region as intensity images. Surface detection and multiple filters were applied to increase image quality.

Section 3.2 Cortex surface detection

Cortex surface is a curve surface. The characterization of optical properties in subsurface region relies on the relative axial distance between cortex surface and the region

of interest. Therefore, the depth of cortex surface in each A-line needs to be determined and the void region above should be removed. Since there is usually strong reflection from cortex surface because of the large difference of index of refraction between air and brain cortex, the surface in attenuation coefficient image presents a bright line which makes surface detection easier. Instead of commonly used edge detection method in typical image processing, I calculated the surface based on the attenuation coefficient depth profile of each A-line and then smoothed the surface array with a 1-D mean filter.

As shown in Figure 3.4, attenuation coefficient of an A-line (vertical line in red) is plotted. The depth index of surface can be found in the first few peaks in the attenuation coefficient depth profile. The surface should be in the top half of the image due to the imaging setting, so only peaks in the depth range of 1 ~ 350 pixels were analyzed. This eliminates the influence from low SNR in the bottom of image. The variance of the first 300 attenuation coefficients was calculated to determine the threshold that helped locate the exact peak with the highest attenuation. The depth position (index) of the peak is assumed to be the surface of the A-line. An array of surface indices from all A-lines in the frame is created and mean filter is performed to smooth the surface curve. Images with detected surface are shown in Figure 3.5.

The optical properties characterization of biological sample, such as mouse brain, focuses on relative depth between region of interest (ROI) and surface. In this example, we took the corpus callosum into analysis. The depth of corpus callosum would be the distance

between corpus callosum and cortex surface instead of the absolute depth on the image. The void region above the surface needs to be cut off based on surface array. Figure 3.5 (d) is a result of attenuation coefficient image with empty region removed. The surface is flattened and all information is shifted to top.

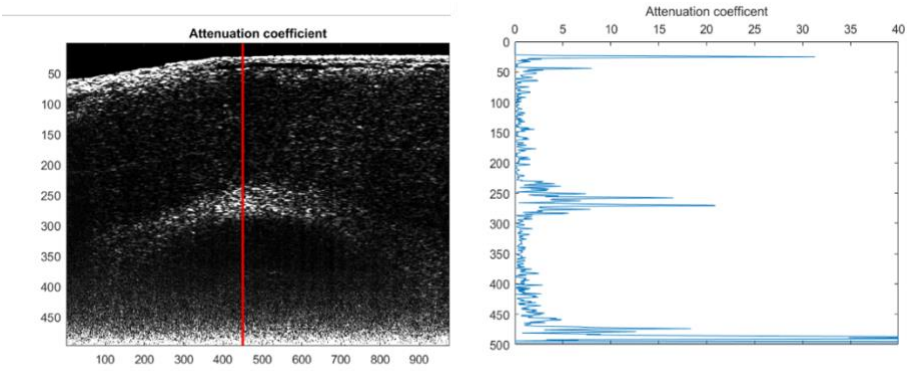

Figure 3.4 The principle of A-line attenuation-based surface detection method. The attenuation coefficients of an A-line (marked as the red line) as a function of depth is plotted. The first high-attenuation region is the cortex surface. Surface depth can be achieved by finding the highest peak. The second high-attenuation region is corpus callosum. Corpus callosum is in deeper region and usually has lower attenuation coefficients than surface.

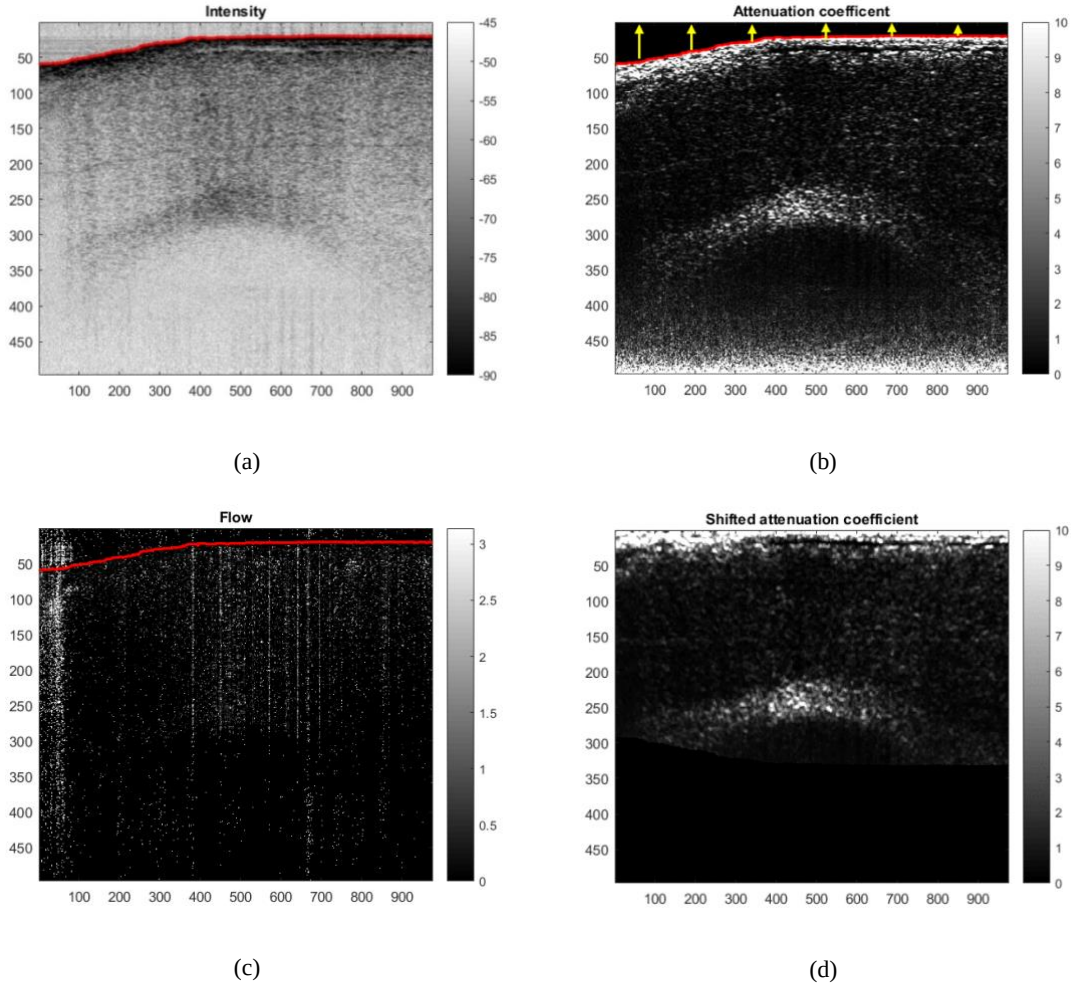

Figure 3.5 Surface indices from all A-lines in the frame form an array. A 1D mean filter is used to the surface array to smooth the detected surface boundary. The result of surface detection is applied to all three types of images. (b) According to surface detection, the void region above surface is removed and surface is flattened. The whole image is shifted to the top as in (d) (bottom part is cut).

Section 3.3 Two-step noise reduction on flow images

En face flow images with cerebral vascular pattern are used in lateral registration. An *en face* flow image is the top view of the projection of flow in different depth layers in a 3D volume with 200 frames. It was obtained by the mean of cortex region along a depth of

21 ~ 100 pixels after the void top region removed. However, the coherent speckle noise was tremendously high that limited the accuracy of registration (Figure 3.6 (a)). [15] I designed a two-step filtering method to reduce the speckles.

Section 3.3.1 Gaussian filter on single frame

A single cross-sectional flow frame does not show distinguishable vessel pattern. Further analysis showed that speckle noise dots on the flow image are random distributed and their pixel values are low. The blood flow information is represented by clusters or lines of connected dots with higher pixel value. In this case, a 3D Gaussian filter would be ideal because Gaussian filter has better performance in preserving those clusters and dots, but 3D filters involve much more computational work. Therefore, a 2D 5×5 Gaussian filter with standard deviation of 5 was applied to each frame. Since the pixel value of most speckles is low, a threshold on histogram was set that forced any pixel with value smaller than it down to zero. The *en face* image after Gaussian filter is shown in Figure 3.6 (b).

Section 3.3.2 Median filter on en face image

Speckle noise on *en face* flow image was significantly reduced after the modified Gaussian filter. However, some strong speckle dots remained. Figure 3.6 (b) shows that these dots are individually distributed but with high pixel value. They can only be blurred by a Gaussian filter rather than be eliminated. A 5×5 median filter was employed because median filters have good behaviors in reducing the effects from small, discrete but strong

noise. After median filter on the *en face* flow image, the pattern of cerebral vessels was revealed. (Figure 3.6 (c))

(a)

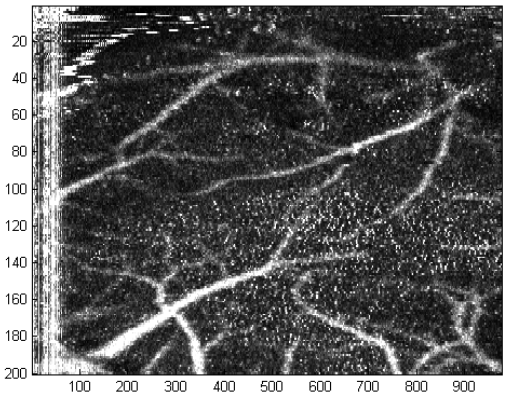

(b)

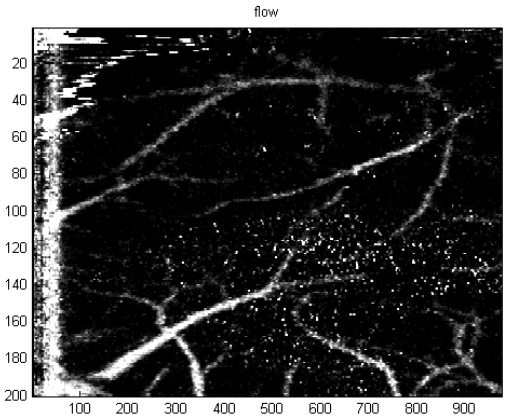

(c)

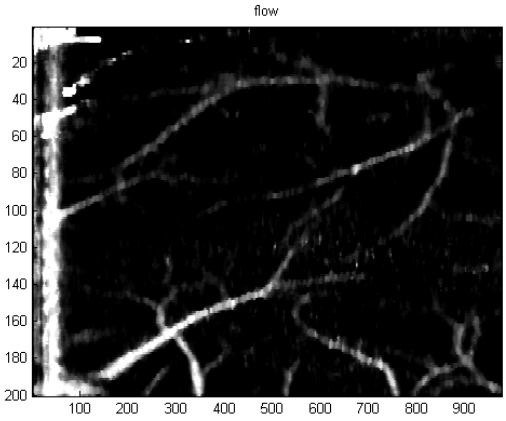

Figure 3.6 *En face* flow images after two step filtering. (a) Original image before filtering. Speckle noise is shown as discrete but dense white dots. (b) *En face* flow image after Gaussian filtering on each frame. Most of the speckles are filtered out except those with high pixel index value. (c) *En face* flow image after median filtering on (b). Clear vessel pattern can be seen.

Section 3.4 *En face* flow images transverse registration

Section 3.4.1 Principle of image registration

Figure 3.7 is a pair of *en face* flow images of the same mouse cortex generated from data taken on Day 0 and Day X. Both images were processed according to Section 3.2 ~ 3.3. The similarity of blood vessel morphological structure between both images can be seen (in yellow boxes). So cross-correlation registration method can be used to handle this registration problem.

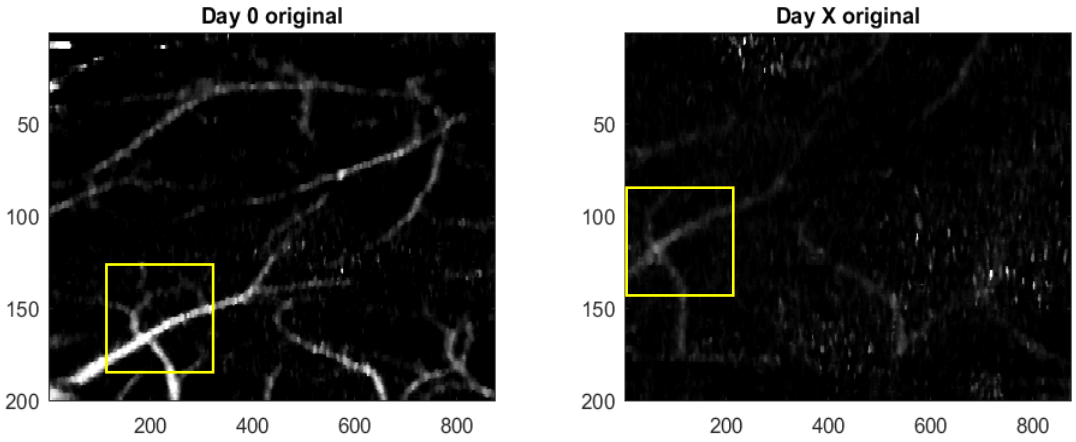

(a) (b)

Figure 3.7 A pair of *en face* flow images from data taken on the same mouse at various time points. This image pair is used in transverse registration. The similar "cross" pattern (in yellow box) on both images shows one of the identical features in the same region.

Cross-correlation is the one of the basic and easily-approachable registration methods that is often used in template matching or pattern recognition. [15] It calculates the degree of similarity between an image and its template. For an image I and a template T, the two-dimensional normalized cross-correlation map C can be expressed as

$$C(u,v) = \frac{\sum_x \sum_y T(x,y) I(x-u, y-v)}{\sqrt{\sum_x \sum_y I^2(x-u, y-v)}} \quad \text{Eq. 3.4}$$

According to Cauchy-Schwarz inequality, it can be inferred that if the image pattern matches the template exactly at a translation of (*i*, *j*), the peak on the cross-correlation map will be at *C*(*i*, *j*). [16] Therefore, the amount of shift, or the degree of similarity, can be determined by computing cross-correlation for all possible translation vectors.

In MATLAB processing, a simple way to approach all possible translations for cross-correlation mapping is based on the Correlation theorem, which states that the Fourier transform of the correlation of two images is the product of the Fourier transform of one image and the complex conjugate of the Fourier transform of the other. [15]

$$\mathcal{F}[C(u,v)] = \mathcal{F}[T(u,v)] \cdot \left[\mathcal{F}[I(u,v)]\right]^* \quad \text{Eq. 3.5}$$

This theorem makes the image registration process computational-efficient and greatly increases the speed for computer to process. And the translation vector is obtained by calculating the offset of peak location to the center. This translation vector indicates the direction and the amount of displacement that the image needs to align with the template.

Section 3.4.2 Method and results

By using the Correlation theorem, the mesh plot of cross-correlation between images in Figure 3.8 can be calculated as shown in Figure 3.8 (a). The translational vector is marked as a red arrow in the image of *x-y* plane view on the right side. The same translation vector is displayed in Figure 3.8 (b) as to indicate the shift direction and displacement to

match Day X (image) to Day 0 (template). The registration result is shown in Figure 3.8 (c).

Since cross-correlation registration method is sensitive to noise [15] and tremendous speckle noise on some of the *en face* flow images may lead to an incorrect peak in cross-correlation map. I included an option of local transverse registration that performs cross-correlation registration on user-selected regions on both images. These regions were rectangular and cropped out from original images. The pixel in top left corner on both cropped regions was set as reference point and based on the reference point, the regions were further cropped to the same size as images to be aligned. The second cropping fixed the size mismatch problem due to user's manual operation. After the cross-correlation registration on the two local images, a translation vector of local images alignment is obtained. The translation vector of the initial images can be calculated by the vector operation on the local translation vector and the offset between the reference points. In this local transverse registration method, high noise region was not involved in the cross-correlation computation process if not selected by user, so the chance of mismatch was reduced.

The result from *en face* flow image transverse registration was applied to the whole depth range and the other types of 3D volumetric images. Therefore, the corresponding intensity and attenuation volumes were laterally aligned. The alignment on attenuation

coefficient volume is especially important because the sequential axial alignment would be mostly based on that as well as optical characterization of biological sample.

(a)

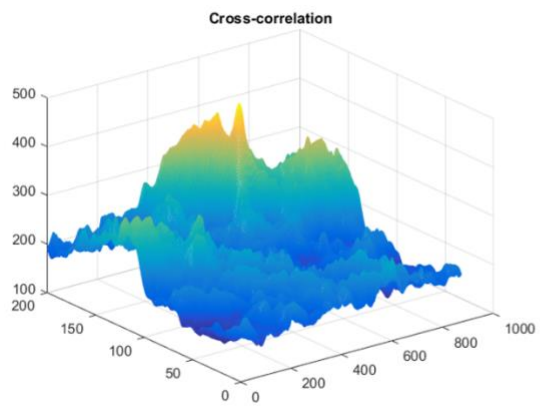

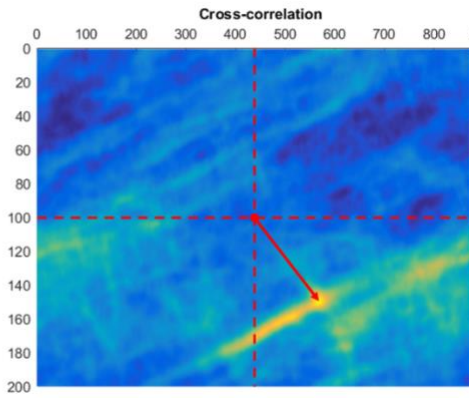

(b)

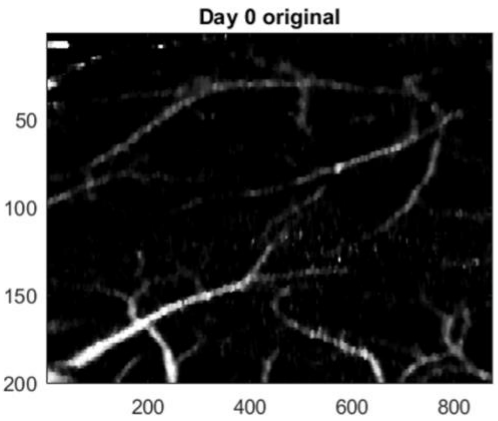

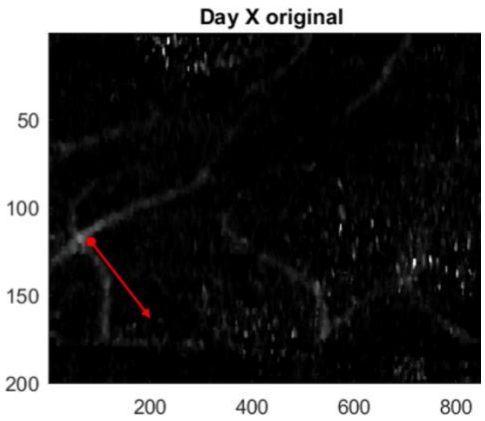

(c)

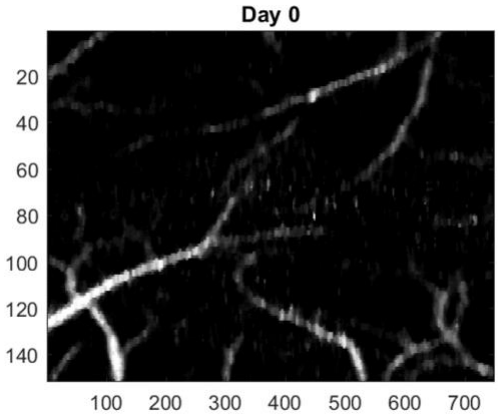

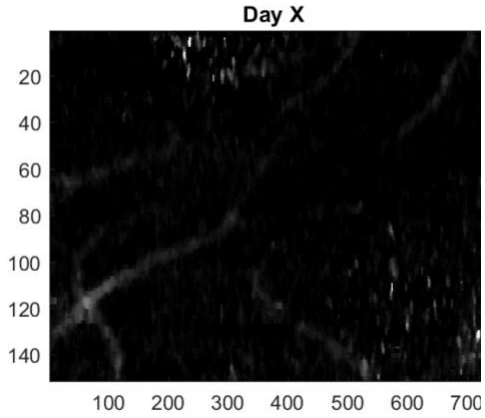

Figure 3.8 Cross-sectional image registration method. (a) A mesh plot of cross-correlation between (b) Day 0 en face flow image as template and Day X as image. The peak of the mesh plot indicates the direction and distance that Day X image needs to shift to match Day 0 template. The right side is the map of the cross-correlation distribution. A translation vector (red arrow) can be obtained by connecting the center point to the peak location. In (b), Day X image is shifted along the same translation vector. (c) shows the result of transverse registration. The "cross" feature marked in yellow boxes in Figure 3.7 is aligned.

Section 3.5 Depth-dependent attenuation coefficient alignment for axial registration

Axial alignment requires clearly identical features along depth. Cross-sectional frames taken from different scanning positions provide depth-resolved information. However, the flow image of mouse cortex as shown in Figure 3.2 (c) does not show nice image pattern. Axial feature can be identified in intensity image, but the gray scale of a deep ROI can be greatly affected by high reflectance of reflectors above it (Figure 3.2 (a)). Less light power will penetrate through the high reflective layers and the deep ROI will look faint. The attenuation coefficient image is reflection of intensity change rate over depth, which can compensate this image pattern loss. In Figure 3.2 (b), clear cortex surface and corpus callosum can be seen.

Mouse brain OCT scanning is conducted in *in vivo* experiments. Mouse growth and experimental treatment during the time between two consequent imaging leads to size changes of brain structures, such as the thickness of cortex and depth of corpus callosum. This change can be found in Figure 3.9 (c), a plot of local attenuation coefficient mean value as a function of depth. The peaks in green region represents the axial position corpus callosum imaged on Day 0 (blue curve) and a later Day X (red curve, here day 30 data was plotted). The mismatch of the two peaks on *x*-axis indicates that there was axial motion in cerebral cortex and corpus callosum.

The local region to be analyzed was selected on the *en face* corpus callosum layer (corresponding to green zone in Figure 3.9 (c)) of the lateral aligned volumes. Corpus

callosum has high attenuation coefficient so that proper size of bright regions in Figure 3.9 (a) and (b) was selected from Day 0 and Day X separately. The selection was made manually so that the cropped regions location (red and blue boxes in Figure 3.9 (a) and (b)) are usually not in exact same size or at exact same. The actual selected region to be analyzed was determined by computing the intersection in the two cropping boxes as shown in green box. Mean value of attenuation coefficient from each *x-y* layer was calculated and the depth-dependent attenuation coefficient plots were obtained (Figure 3.9 (c)).

On the plot in Figure 3.9 (c), each curve has a high attenuation region of cerebral surface (red zone) and a relatively high attenuation peak of corpus callosum in deeper region. The region between surface and corpus callosum is low-attenuated cortex which does not show statistical features. The regions on the curves that can be used to locate corresponding depths are surface zone the corpus callosum zone. Therefore, two reference points are selected on each curve, the reflection between surface and cortex, and the attenuation peak on corpus callosum. The first reference (marked as "star") point is determined by finding the end point in an array of all points with attenuation coefficient over 2 in the depth range between 1 and 50 (array index unit). The second reference point (marked as "triangle") is obtained from the maximum of 4^{th} order polynomial fit of the peak. The rest alignment strategy is then to anchor those reference points and normalize the distance between inflection point and corpus callosum peak. Interpolation method is involved in re-assigning the correct depth index in MATLAB processing.

The result of axial alignment is shown in Figure 3.9 (d). The corpus callosum from data taken at different time points are now in the same depth. This makes optical characterization of brain biological features at various time comparable. For example, the attenuation coefficient of corpus callosum in later time point Day X is higher than that in initial time point Day 0. Knowing the relative change in optical properties helps collaborating research team understand the progression of a certain disease or effects due to their experimental treatment in a different aspect. This may provide potential ways in disease diagnosis or the improvement of biological-related experiments.

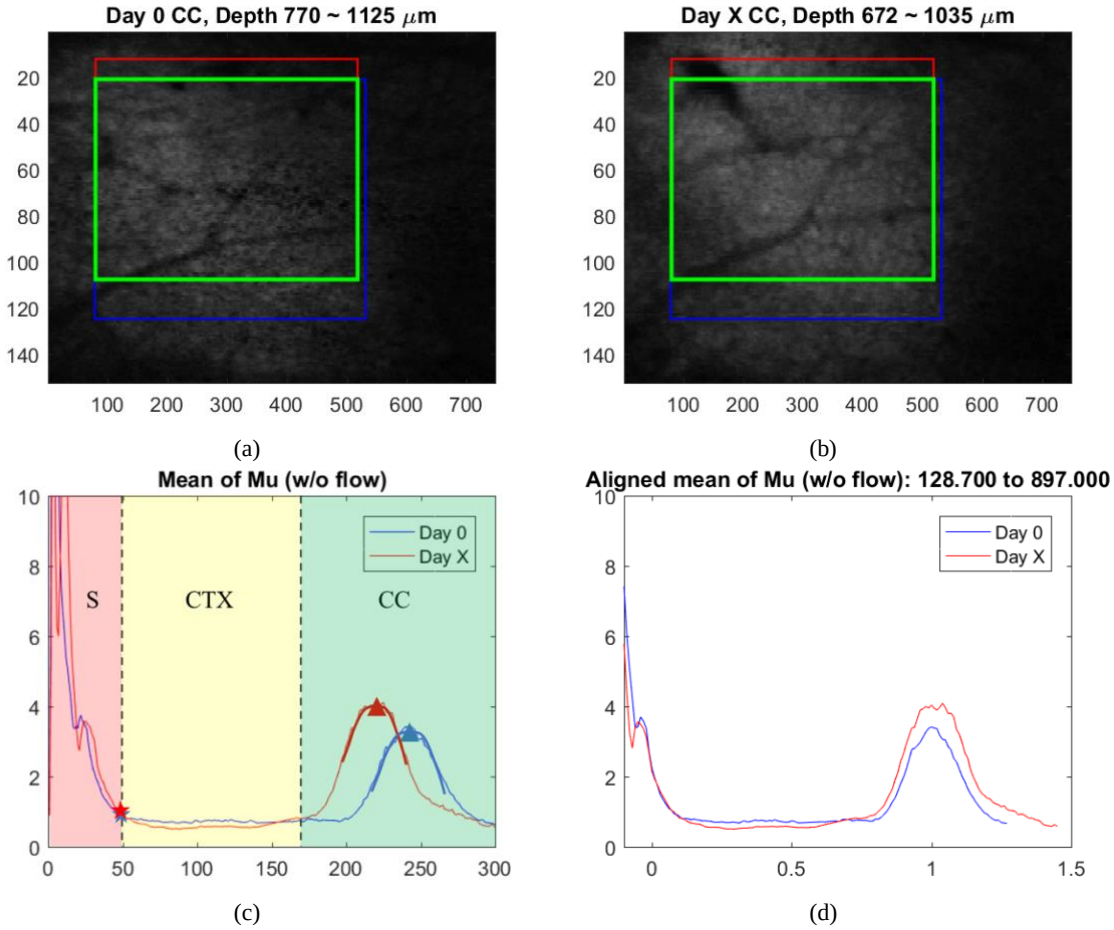

Figure 3.9 Attenuation coefficient-based axial alignment. (a) and (b) are *en face* images of corpus callosum zone (green zone in (c)). The bright part is corpus callosum where the cropping boxes are selected on each image. The selected region on Day 0 is marked as blue box and Day X as red box. The region to be analyzed is the intersection of two boxes, marked in green. (c) is a plot of attenuation coefficient curves versus depth. It is roughly divided into three zones in different colors, surface zone in red, cerebral cortex zone in yellow and corpus callosum zone in green. The reference points for axial alignment are denoted as "stars" (reflection on the curve between surface and cortex zone) and "triangles" (peaks in corpus callosum zone). The aligned curves are shown in (d). The two peaks in corpus callosum match and the on taken on Day X has higher light attenuation.

Chapter 4 Post-Processing Application in *in vivo* Mouse Brain Imaging

Section 4.1 Optical characterization of post-traumatic epilepsy (PTE)

Section 4.1.1 Introduction

Traumatic brain injury is a heterogeneous disorder and it has been a major cause of morbidity and mortality in people under the age of 45. [18] A secondary injury of traumatic brain injury leads to the development of epilepsy where neural circuitry reorganization transpires into permanent hyperexcitability and the manifestation of spontaneous recurrent seizures. [19] This post-traumatic epilepsy (PTE) occupies 6% of all kinds of epilepsy. [20] Understanding the mechanisms of PTE has significance in preventing PTE occurrence on patients suffering from traumatic brain injury.

Current modalities of PTE characterization depend on video electroencephalographic (V-EEG) and magnetic resonance imaging (MRI). VEEG monitors and quantitatively identifies spontaneous seizure. [21] Diffusion-weighted MRI is feasible to associate hippocampal damage to increased seizure susceptibility in animals that have undergone traumatic brain injury, but the correlation between cortical damage and seizure susceptibility is not observed. [22] To investigate the pathophysiology of brain trauma-induced spontaneous seizure, OCT-based optical properties characterization is involved because of its high-resolution, label-free and minimally-invasive nature. [10][17] Our collaborating research team in the Biomedical Sciences program and the Department of Neuroscience at University of California, Riverside set hypotheses on the correlation

between traumatic epileptogensis in mouse model and hippocampal histopathology, and attempt to reveal optical biomarkers based on OCT images that have potential meanings in PTE mechanism research.

Section 4.1.2 Characterization of PTE in various imaging time points

The imaging portion of this series PTE experiments was performed on 1310 SD-OCT system (Figure 4.1). The skull of each mouse was removed prior the imaging. Initial *in vivo* mouse brain models (Day 0) was imaged in 3D volumes as control groups. The mice were treated based on neuroscience research purposes. At a later day point (Day X), the corresponding mouse brain was scanned again on the same region. 3D volume registration method introduced in Chapter 3 was performed in OCT data post-processing.

The optical properties change, such as light attenuation and flow density, in corresponding regions from two scanning time points was then compared and analyzed. Light attenuation change is displayed in the same manner as the plot I used to align depth information (Figure 3.9 (d)). A plot of attenuation of Day X to Day 0 ratio versus depth is added for better tracking the attenuation change in cerebral cortex and corpus callosum. Flow density represents cerebral blood flow rate during the scanning. Based on the cross-sectional flow frames and *en face* flow image, a 3D binary mask of blood vessel image can be obtained by using proper image edge detection methods (here I used image dilation and erosion with proper phase difference value threshold). This binary mask is able to pick out all blood vessel pixels with corresponding phase difference values. Flow density is

calculated by summing or averaging the phase difference, and flow density change is the ratio of flow densities from two time points. Two examples of characterization result are shown in Figure 4.2 and Figure 4.3. These data were taken from two mice in 20 days treatment (Figure 4.2) and 90 days treatment (Figure 4.3), respectively. Both sets of 3D volumes are well-aligned in lateral and axial directions as illustrated in (a) (b) and (c).

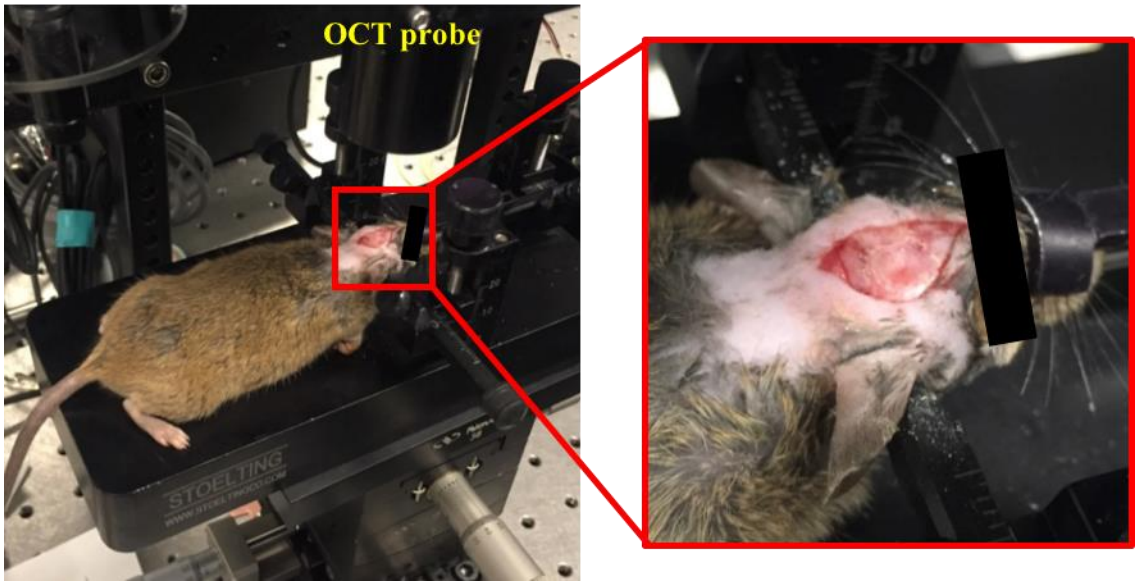

Figure 4.1 PTE experiment setup. The skull of mouse was removed properly before experiment. The region to be scanned is placed under the center OCT sample probe and on the focal plane of sample lens. Image on the right is a zoom-in image of the region on brain that needs to be scanned.

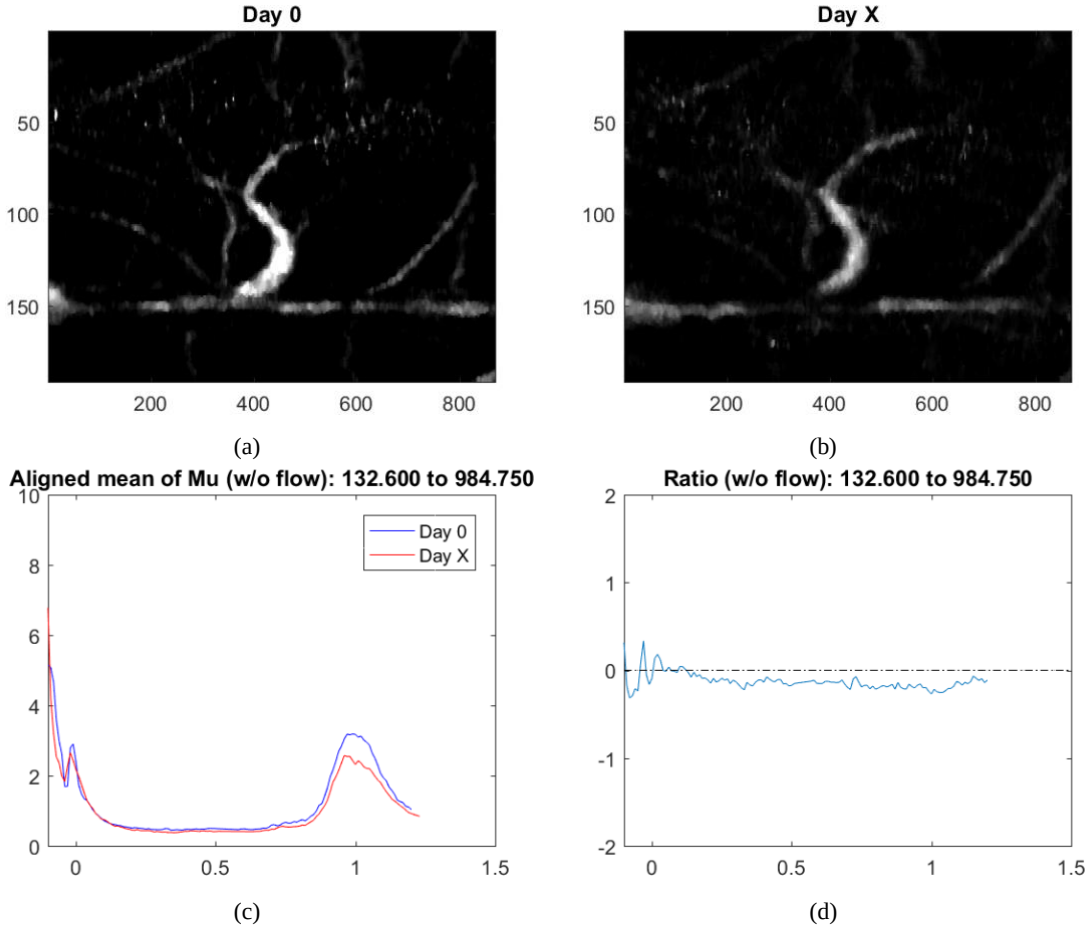

Figure 4.2 An example of optical characterization of mouse in 20 days treatment (Day 0: 2016/09/27, Day X: 2016/10/17). *En face* flow images in (a) and (b) have been shifted after lateral registration. The "S" shape vessel on the two images match each other in the same position. Attenuation peaks in (c) align each other well. Ratio of attenuation coefficient versus depth is plotted in (d). Flow density (mean value): Day 0, 57.9256; Day X: 53.7817. Flow density ratio: 1.0770.

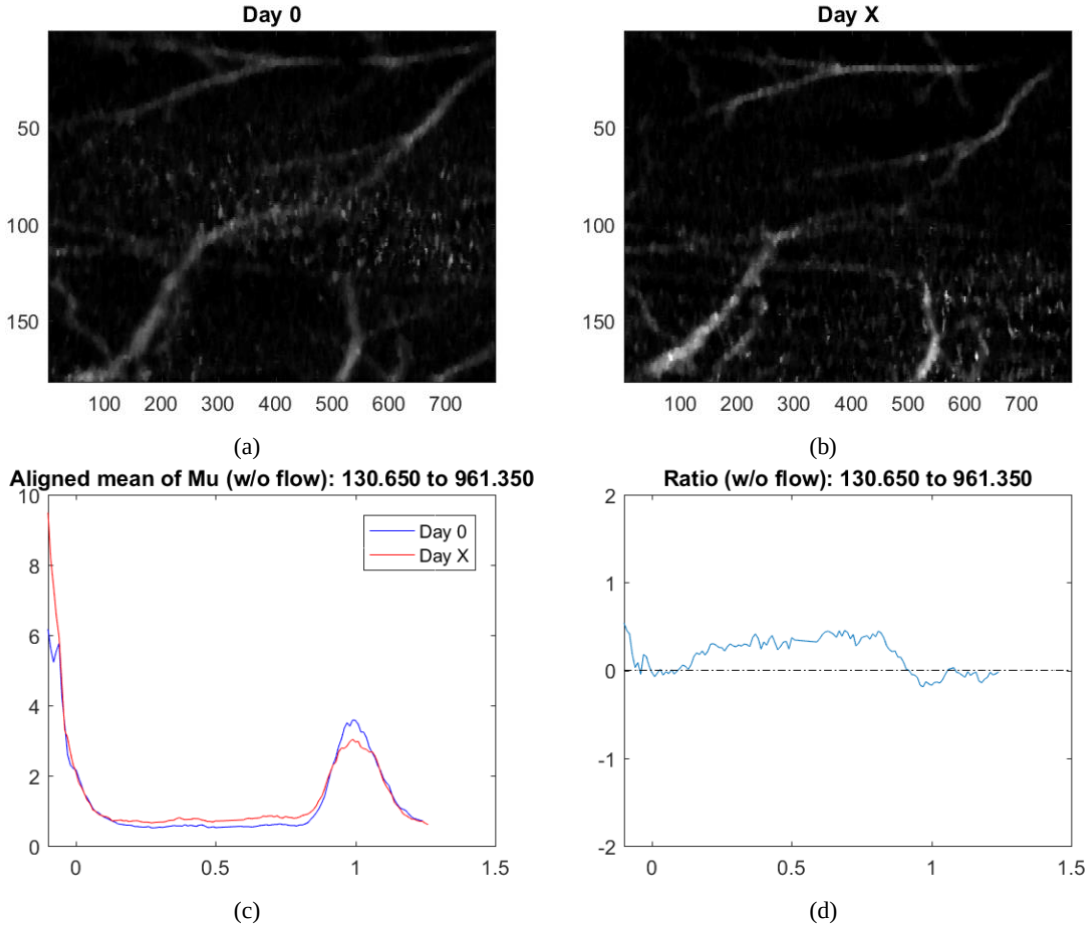

Figure 4.3 An example of optical characterization of mouse in 90 days treatment (Day 0: 2016/11/04, Day X: 2017/01/23). Flow density (mean value): Day 0, 36.5077; Day X: 39.8041. Flow density ratio: 0.9172.

Section 4.2 Window to the Brain (WttB) implant experiment

Optical experimental and diagnostic procedures have been widely applied in a series of collaborating research projects. Optical signal from OCT sample arm can be significantly hindered by high scattering cranial bone such as skull. Therefore, craniotomy (removal of a section of skull) becomes necessary to provide optical access each time an OCT experiment is performed. Repeated surgeries for each scanning introduce uncertainty to optical characterization and increase the risk to the mice or patient. One potential way to overcome this limitation is to introduce a transparent cranial implant (We call the Window to the Brain, WttB) that has optimal optical features as well as protects the brain and prevents structural change due to the growth of skull. It has been demonstrated that an implant made of nanocrystalline yttria stabilized zirconia (nc-YSZ) can improve OCT image SNR and contrast. [23]

Figure 4.4 (a) is the comparison of image quality and signal level of murine brain through WttB implant (flat surface on left side) and native cranium (right tilted region). The image contrast under WttB implant is better compared to the right native skull region. Figure 4.4 (b) is the average of depth profiles in the corresponding region between dash lines. The signal received is enhanced under the implant.

Advanced investigation is performing on five mouse models at multiple subsequent time points over 30 days. More details of the optical feature of the implant will be examined including light incident angle. Figure 4.5 shows the imaging setup of WttB experiments. A

pair of goniometric stages were added to ensure each time the incident angle remained the same. This is because the power of light refracted by two boundaries of the implant (between air and implant, and between implant and cortex) is dependent on the incident angle.

The same volumetric registration method will be applied on the post-processing 3D volume comparison upon needed. Blood flow will be mapped across the WttB implant over corresponding time points. The future direction of this collaborating work towards a viable transparent implant to compensate OCT performance and increase image quality. Success demonstration of this implant will lead to broader applications in optical neurological study and cerebral disease diagnosis.

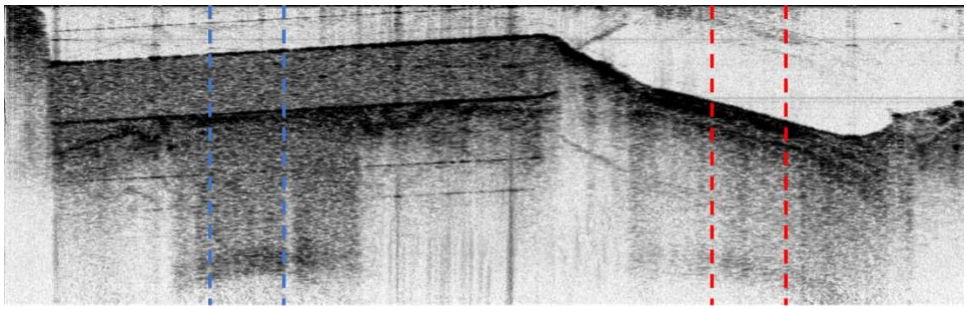

(a)

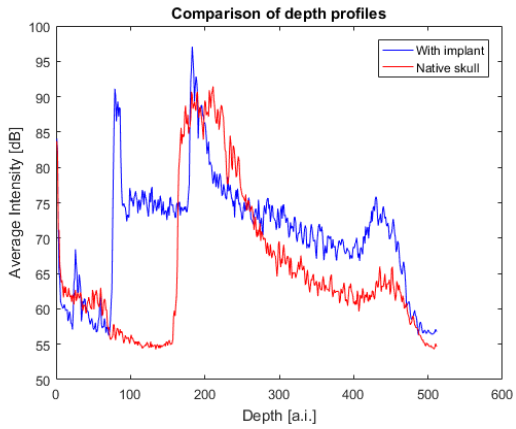

(b)

Figure 4.4 Comparison of image quality and signale intensity between zones with implant and native skull. Depth profiles are calculated from regions between dash lines in (a). Both (a) and (b) show that there was more power received under WttB implant and thus the contrast was enhanced.

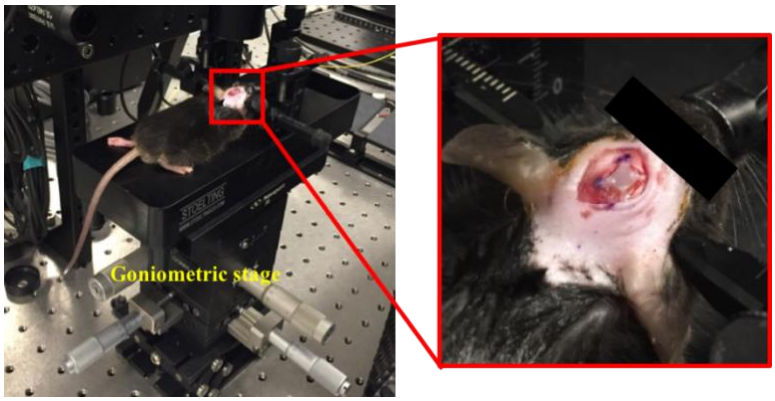

Figure 4.5 WttB experiment setup with goniometric stages. The chip on the surface of murine brain is the nc-YSZ implant.

References

[1] Huang, D., Swanson, E. A., Lin, C. P., Schuman, J. S., Stinson, W. G., Chang, W., ... & Fujimoto, J. G. (1991). Optical coherence tomography. *Science (New York, NY)*, *254*(5035), 1178.

[2] Drexler, W., & Fujimoto, J. G. (2015). *Optical coherence tomography: technology and applications*. Springer.

[3] Akcay, C., Parrein, P., & Rolland, J. P. (2002). Estimation of longitudinal resolution in optical coherence imaging. *Applied optics*, *41*(25), 5256-5262.

[4] De Boer, J. F., Cense, B., Park, B. H., Pierce, M. C., Tearney, G. J., & Bouma, B. E. (2003). Improved signal-to-noise ratio in spectral-domain compared with time-domain optical coherence tomography. *Optics letters*, *28*(21), 2067-2069.

[5] Wang, Y., Oh, C. M., Oliveira, M. C., Islam, M. S., Ortega, A., & Park, B. H. (2012). GPU accelerated real-time multi-functional spectral-domain optical coherence tomography system at 1300nm. *Optics express*, *20*(14), 14797-14813.

[6] Mujat, M., Park, B. H., Cense, B., Chen, T. C., & de Boer, J. F. (2007). Autocalibration of spectral-domain optical coherence tomography spectrometers for in vivo quantitative retinal nerve fiber layer birefringence determination. *Journal of biomedical optics*, 12(4), 041205-041205.

[7] Wojtkowski, M., Leitgeb, R., Kowalczyk, A., Bajraszewski, T., & Fercher, A. F. (2002). In vivo human retinal imaging by Fourier domain optical coherence tomography. *Journal of biomedical optics*, *7*(3), 457-463.

[8] Gaylord, T. K., & Moharam, M. G. (1985). Analysis and applications of optical diffraction by gratings. *Proceedings of the IEEE*, 73(5), 894-937.

[9] M. Wojtkowski, R. Leitgeb, A. Kowalczyk, T. Bajraszewski, and A. F. Fercher, "*In vivo* human retinal imaging by Fourier domain optical coherence tomography," *J. Biomed. Opt.* **7** 3 , 457–463 2002 .

[10] Rodriguez, C. L., Szu, J. I., Eberle, M. M., Wang, Y., Hsu, M. S., Binder, D. K., & Park, B. H. (2014). Decreased light attenuation in cerebral cortex during cerebral edema detected using optical coherence tomography. *Neurophotonics*, *1*(2), 025004-025004.

[11] Park, B. H., Pierce, M. C., Cense, B., Yun, S. H., Mujat, M., Tearney, G. J., ... & de Boer, J. F. (2005). Real-time fiber-based multi-functional spectral-domain optical coherence tomography at 1.3 μm. *Optics Express*, 13(11), 3931-3944.

[12] Hartl, I., Li, X. D., Chudoba, C., Ghanta, R. K., Ko, T. H., Fujimoto, J. G., ... & Windeler, R. S. (2001). Ultrahigh-resolution optical coherence tomography using continuum generation in an air–silica microstructure optical fiber. *Optics letters*, 26(9), 608-610.

[13] Park, B. H., Pierce, M. C., Cense, B., Yun, S. H., Mujat, M., Tearney, G. J., ... & de Boer, J. F. (2005). Real-time fiber-based multi-functional spectral-domain optical coherence tomography at 1.3 μm. *Optics Express*, 13(11), 3931-3944.

[14] Vermeer, K. A., Mo, J., Weda, J. J. A., Lemij, H. G., & De Boer, J. F. (2014). Depth-resolved model-based reconstruction of attenuation coefficients in optical coherence tomography. *Biomedical optics express*, 5(1), 322-337.

[15] Brown, L. G. (1992). A survey of image registration techniques. *ACM computing surveys* (CSUR), 24(4), 325-376.

[16] Rosenfeld, A., & Kak, A. C. (1982). *Digital picture processing*, vol. 2.

[17] Eberle, M. M., Hsu, M. S., Rodriguez, C. L., Szu, J. I., Oliveira, M. C., Binder, D. K., & Park, B. H. (2015). Localization of cortical tissue optical changes during seizure activity in vivo with optical coherence tomography. *Biomedical optics express*, *6*(5), 1812-1827.

[18] Pitkänen, A., & Mcintosh, T. K. (2006). Animal models of post-traumatic epilepsy. *Journal of neurotrauma*, *23*(2), 241-261.

[19] Ren, Z., Iliff, J. J., Yang, L., Yang, J., Chen, X., Chen, M. J., ... & Nedergaard, M. (2013). 'Hit & Run'model of closed-skull traumatic brain injury (TBI) reveals complex patterns of post-traumatic AQP4 dysregulation. *Journal of Cerebral Blood Flow & Metabolism*, *33*(6), 834-845.

[20] Kendirli, M. T., Rose, D. T., & Bertram, E. H. (2014). A model of posttraumatic epilepsy after penetrating brain injuries: effect of lesion size and metal fragments. *Epilepsia*, *55*(12), 1969-1977.

[21] Hudak, A. M., Trivedi, K., Harper, C. R., Booker, K., Caesar, R. R., Agostini, M., ... & Diaz-Arrastia, R. (2004). Evaluation of Seizure-like Episodes in Survivors of Moderate and Severe Traumatic Brain Injury. *The Journal of head trauma rehabilitation*, *19*(4), 290-295.

[22] Immonen, R., Kharatishvili, I., Gröhn, O., & Pitkänen, A. (2013). MRI biomarkers for post-traumatic epileptogenesis. *Journal of neurotrauma*, *30*(14), 1305-1309.

[23] Damestani, Y., Reynolds, C. L., Szu, J., Hsu, M. S., Kodera, Y., Binder, D. K., ... & Aguilar, G. (2013). Transparent nanocrystalline yttria-stabilized-zirconia calvarium prosthesis. *Nanomedicine: Nanotechnology, Biology and Medicine*, *9*(8), 1135-1138.